Falling cards

By MARVIN A. JONES[1] AND MICHAEL J. SHELLEY[2]

[1]Department of Applied Mathematics and Theoretical Physics, University of Cambridge,
Centre for Mathematical Sciences, Wilberforce Road, Cambridge, CB3, 0WA, UK

[2]Courant Institute of Mathematical Sciences, New York University,
251 Mercer St., New York, NY 10012, USA

In this study we consider the unsteady separated flow of an inviscid fluid (density ρ_f) around a falling flat plate (thickness T, half-chord L, width W, and density ρ_s) of small thickness and high aspect ratio ($T \ll L \ll W$). The motion of the plate, which is initially released from rest, is unknown in advance and is determined as part of the solution. The flow solution is assumed two-dimensional and to consist of a bound vortex sheet coincident with the plate and two free vortex sheets that emanate from each of the plate's two sharp edges. Throughout its motion, the plate continually sheds vorticity from each of its two sharp edges and the unsteady Kutta condition, which states the fluid velocity must be bounded everywhere, is applied at each edge. The coupled equations of motion for the plate and its trailing vortex wake are derived (the unsteady aerodynamic loads on the plate are included) and are shown to depend only on the modified Froude number $Fr = T\rho_s/L\rho_f$. Crucially, the unsteady aerodynamic loads are shown to depend on not only the usual acceleration reactions, which lead to the effect known as added mass, but also on novel unsteady vortical loads, which arise due to relative motion between the plate and its wake. Exact expressions for these loads are derived.

An asymptotic solution to the full system of governing equations is developed for small times $t > 0$ and the initial motion of the plate is shown to depend only on the gravitational field strength and the acceleration reaction of the fluid; effects due to the unsteady shedding of vorticity remain of higher order at small times.

At larger times, a desingularized numerical treatment of the full problem is proposed and implemented. Several example solutions are presented for a range of modified Froude numbers Fr and small initial inclinations $\theta_0 < \pi/32$. All of the cases considered were found to be unstable to oscillations of growing amplitude. The non-dimensional frequency of the oscillations is shown to scale in direct proportion with the inverse square root of the modified Froude number $1/\sqrt{Fr}$. Importantly, the novel unsteady vortical loads are shown to dominate the evolution of the plate's trajectory in at least one example. Throughout the study, the possibility of including a general time-dependent external force (in place of gravity) is retained.

1. Introduction

Here the problem of determining the unsteady separated flow of an inviscid fluid around a freely falling flat plate is considered and solved in two dimensions using a boundary integral formulation. The problem represents perhaps the simplest example of an inertial-fluid–free-boundary problem; that being a problem in which a massive

free boundary is forced to interact with an incompressible fluid at high Reynolds number.

Such interactions occur throughout the natural world, in particular wherever biological systems come into contact with fluids. However, they are perhaps most apparent in the field of animal locomotion. In such situations the role of the inertial free boundary is played by the organism itself, be it a swimming fish or a hovering insect, and the interaction between the organism and the surrounding fluid is typically harnessed to provide an efficient means of propulsion. Generically, the organism in question will actively create a disturbance in the fluid immediately surrounding itself and will experience a corresponding reaction. At the moderately high Reynolds numbers relevant here, these disturbances are most commonly manifested as concentrated vortices that are subsequently shed into a vortical wake. Our ultimate goal is to understand the underlying mechanisms at work in such situations, with particular emphasis on gaining insight into the interaction between the organism and its wake. Identical interactions occur, albeit passively, within the context of the falling card problem; as the card falls it creates a vortical wake, which in turn influences the card's downward trajectory. Because of this, we adopt the simpler falling card problem as our paradigm.

To date there have been many investigations into variants of the falling card problem. In an early paper, Maxwell (1853) made several detailed and insightful observations on the subject of falling rectangular slips of paper. He began, "Every one must have observed that when a slip of paper falls through the air, its motion, though undecided and wavering at first, sometimes becomes regular." Much later Willmarth, Hawk & Harvey (1964) performed a beautiful set of experiments with freely falling disks and confirmed Maxwell's observations. At high Reynolds number, they found that, as they fell, the disks exhibited either "regular pitching and translational oscillations", or alternatively, "tumbled in an apparently random manner", with tumbling occurring for disks with a non-dimensional moment of inertia above a critical value. In a more recent study Field *et al.* (1997) identified an additional class of chaotic motions for moments of inertia near to the critical value. For rectangular cards, Belmonte, Eisenberg & Moses (1998) took special care to study the two-dimensional aspects of the problem at high Reynolds number and identified a transition from fluttering to tumbling at a critical modified Froude number (the modified Froude number plays essentially the same role as the non-dimensional moment of inertia). Soon after, Mahadevan, Ryu & Samuel (1999) considered freely tumbling plastic strips of high aspect ratio and used dimensional arguments to provide a scaling for the average rate of descent and the tumbling frequency. Recently, investigations based on the numerical solution of the two-dimensional Navier–Stokes equations have also been carried out by Mittal, Seshadri & Udaykumar (2004), who considered a freely falling cylinder with rounded edges, and Pesavento & Wang (2004) and Andersen, Pesavento & Wang (2005), who considered a freely falling elliptical cylinder. A transition from flutter to tumble is again reported as the non-dimensional moment of inertia of the cylinder is increased.

From a more theoretical perspective many authors, including some of those highlighted above and referenced therein, have explored a plethora of low-dimensional dynamical systems that seek to model the complexities of the falling card problem by introducing *ad hoc* approximations for the aerodynamic force and torque on the falling card. In the current study we succeed in completely removing the need for such inventions by properly posing the falling card problem within the context of two-dimensional inviscid theory. A detailed description of the card's vortical wake is incorporated and the loads that arise through the action of the resulting normal
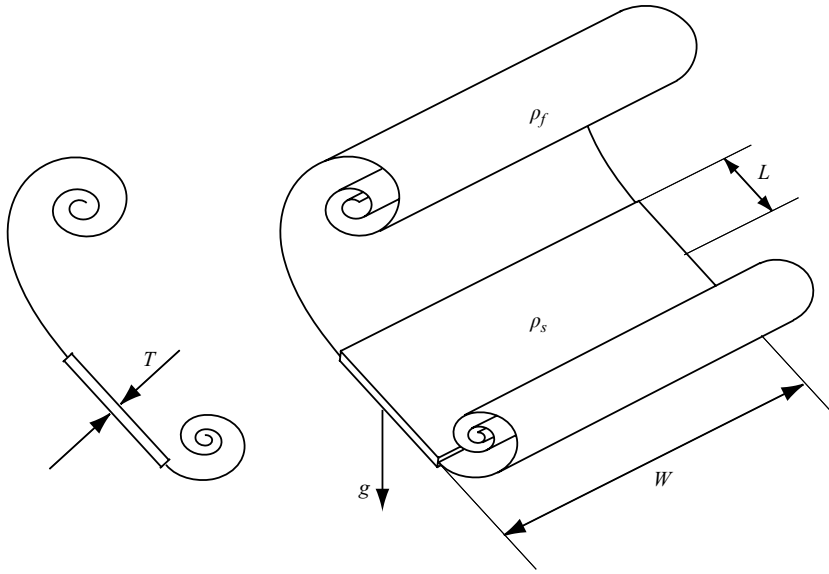
FIGURE 1. A cross-section and three-dimensional diagram of the falling plate and its vortex wake indicating the plate thickness T, half-chord L, width W, plate density ρ_s, fluid density ρ_f and the gravitational field strength g.

pressure forces on the card are included. As a result, we are able to investigate the interaction between the falling card and its vortical wake. Forces associated with viscous shear stresses, which are of order $1/\sqrt{Re} \ll 1$, are neglected.

1.1. *Non-dimensionalization of the governing equations*

The problem is essentially described as follows. A rigid flat plate of chord length $2L$, thickness T, width W, and density ρ_s is placed in a uniform gravitational field of strength g and immersed in a fluid of density ρ_f and kinematic viscosity ν. See figure 1. When released from rest the plate will either rise due to buoyancy, fall under gravity, or remain perfectly still. In what follows, we will consider only the falling case, in which $\rho_s > \rho_f$. As it falls, the motion of the plate will, in general, become complicated, consisting of various three-dimensional fluttering and tumbling motions. However, if we restrict our attention to thin cards of high aspect ratio, such that $T \ll L \ll W$, then we can reasonably expect the motion to remain approximately two-dimensional. The two-dimensional problem retains many of the interesting features of the fully three-dimensional problem, including its interactive nature, but more to the point it is not understood in its own right and is therefore worthy of study.

We begin by non-dimensionalizing the relevant governing equations – the Euler equations and Newton's equations of motion for the plate – using the half-chord length L, the fluid density ρ_f, an as yet undetermined velocity U, and twice the fluid stagnation pressure $\rho_f U^2$. The unknown velocity U is determined by assuming that the gravitational (or otherwise externally prescribed) force on the plate is in rough balance with the aerodynamic force on the plate. In other words, U is taken to be the approximate terminal velocity of the falling plate. This balance also forms the basis of an experimental scaling law studied by Mahadevan *et al.* (1999). The magnitude of the gravitational force on the plate is $2LTW(\rho_s - \rho_f)g$ (the buoyancy force has been included in this estimate) and the magnitude of the aerodynamic force on the

plate is of the order $2LW\rho_f U^2$. A balance therefore provides an estimate for U^2 in the form $Tg(\rho_s - \rho_f)/\rho_f$. (If gravity were absent and a force of magnitude f present instead, then a dominant balance would lead to the estimate $f/2LW\rho_f$ for U^2.)

Having identified the unknown velocity U, only two non-dimensional parameters remain: the Reynolds number $Re = UL/\nu$ and the modified Froude number

$$Fr = \frac{\rho_s}{(\rho_s - \rho_f)}\frac{U^2}{gL} = \frac{m}{2L^2 W\rho_f} = \frac{T\rho_s}{L\rho_f}, \qquad (1.1)$$

where m is the mass of the plate. Since we are considering an effectively inviscid fluid, the Reynolds number is henceforth assumed large, $Re \gg 1$, and consequently does not appear again in our formulation. However, the effects of viscosity are included by allowing discontinuous solutions of the governing Euler equations, in particular solutions containing vortex sheets. Such solutions are considered physically acceptable since the presence of viscosity, however small, is able to smooth the corresponding discontinuities in the real fluid. As a result, and in contrast to the previous theoretical work on the problem, we are able to include the dynamics of the plate's wake in our description of the flow.

In contrast, the modified Froude number remains relevant and has a number of physical interpretations, as alluded to in the equation above. However, within the context of the falling card problem, it seems most natural to interpret it as the ratio of the mass of the plate over the mass of the fluid column immediately surrounding the plate. As such it essentially characterizes the relative importance of plate inertia – the motion of a relatively heavy plate ($Fr \gg 1$) being mostly unaffected by the motion of the fluid; the motion of a relatively light plate ($Fr \ll 1$) being highly dependent on the motion of the surrounding fluid.

2. Problem formulation

We pose the problem in the rest frame of the fluid in the far field and the complex number $z = x + iy$ is used to denote the position of a point in this frame, where x and y are the horizontal and vertical Cartesian components of the point z. The plate is assumed to fall through this frame under the influence of the gravitational and aerodynamic forces in the problem (other external forces may be included) and our task is to determine its exact trajectory, as well as the resulting motion in the surrounding fluid.

2.1. *The motion of the plate*

We use two variables to describe the plate's position and orientation: the position of the plate's centre of mass is denoted using the complex number $c(t)$ and the angle that the plate's tangent makes with the horizontal is denoted $\theta(t)$. For convenience, we also choose to describe the plate parametrically using the complex number $\zeta(s, t)$, where

$$\zeta(s, t) = c(t) + s e^{i\theta(t)}, \qquad (2.1)$$

and s is the signed arc-length as measured along the plate from $c(t)$. In addition, the position of each of the plate's two sharp edges is denoted using the complex numbers $e_\pm(t)$, where
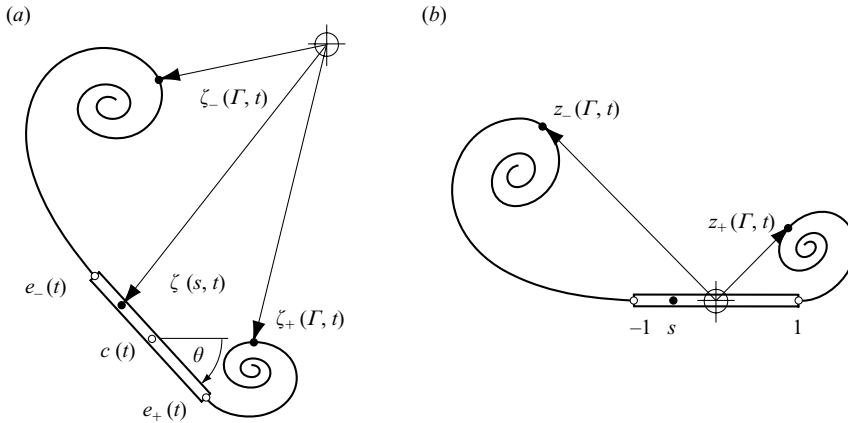
$$e_\pm(t) = c(t) \pm e^{i\theta(t)}. \qquad (2.2)$$

FIGURE 2. The dependent variables in (*a*) the rest frame of the fluid in the far field and (*b*) the body frame. The centre of the plate $c(t)$, the orientation angle $\theta(t)$, the plate edges $e_\pm(t)$, the position of a point on the plate $\zeta(s,t)$, and the position of a point on the shed vortex sheets $\zeta_\pm(\Gamma,t)$ (or $z_\pm(\Gamma,t)$ in the body frame).

See figure 2. Having defined our dependent variables $c(t)$ and $\theta(t)$, we next consider their time evolution. We do this by writing down the equations of motion for $c(t)$ and $\theta(t)$ that result from a consideration of the gravitational and aerodynamic forces on the falling card. In non-dimensional form, the appropriate equations of motion are

$$Fr\,\ddot{c}(t) = F(t) + \tfrac{1}{2}\mathbb{F}(t)\mathrm{i}\mathrm{e}^{\mathrm{i}\theta(t)}, \tag{2.3}$$

$$\tfrac{1}{3}Fr\,\ddot{\theta}(t) = T(t) + \tfrac{1}{2}\mathbb{T}(t), \tag{2.4}$$

where $\mathbb{F}(t)$ is the normal aerodynamic force on the plate and $\mathbb{T}(t)$ is the aerodynamic torque on the plate. In the interests of generality, the gravitational force has been included in the form of the externally prescribed force $F(t)$ and an externally prescribed torque $T(t)$ has also been included. The falling card problem can be recovered by setting $F(t) = -\mathrm{i}$ and $T(t) = 0$. In addition, the relevant moment of inertia of the card has been taken to be $2L^3TW\rho_s/3$, which corresponds to a uniform distribution of mass throughout the plate. A dot has been used to denote differentiation with respect to time. Equations (2.3) and (2.4) confirm that the modified Froude number is an effective inertial constant that characterizes the strength of the interaction between the falling plate and the fluid.

Since the aerodynamic loads $\mathbb{F}(t)$ and $\mathbb{T}(t)$ both depend, in a complicated way, on the plate's position, velocity, acceleration, and general fluid environment it is easy to see that the description of the problem is far from complete. Fortunately, the analysis required to uncover the exact dependence of $\mathbb{F}(t)$ and $\mathbb{T}(t)$ on the other variables in the problem has already been carried out and the reader is referred to the preparatory study by Jones (2003) for a detailed account. The essential definitions and results from Jones (2003) are given here for convenience. Since $Re \gg 1$, the force $\mathbb{F}(t)$ and the torque $\mathbb{T}(t)$ are assumed to take the form

$$\mathbb{F}(t) = -\int_{-1}^{+1} [p_\pm(\lambda,t)]_-^+ \,\mathrm{d}\lambda, \tag{2.5}$$

$$\mathbb{T}(t) = -\int_{-1}^{+1} \lambda[p_\pm(\lambda,t)]_-^+ \,\mathrm{d}\lambda, \tag{2.6}$$

where $[p_\pm(s,t)]_-^+ = p_+(s,t) - p_-(s,t)$ denotes the pressure difference across the plate at the point $\zeta(s,t)$. In turn, the pressure difference $[p_\pm(s,t)]_-^+$ can be expressed, through the use of the Euler equations, in the form

$$[p_\pm(s,t)]_-^+ = -\partial_t \Gamma(s,t) - \gamma(s,t)(\mu(s,t) - \tau(t)), \tag{2.7}$$

where $\gamma(s,t)$ is the jump in the tangential component of the fluid velocity across the plate, $\mu(s,t)$ is the average of the tangential fluid velocities on either side of the plate, and $\tau(t)$ is the tangential component of the plate's velocity. In addition, $\Gamma(s,t)$ is defined as the circulation around a particular closed curve that intersects the falling plate exactly once at $\zeta(s,t)$ (for a more detailed definition of the circulation and the contour used to define it see Jones 2003). However, for our purposes, it is sufficient to note that $\mathrm{d}\Gamma = \gamma(s,t)\,\mathrm{d}s$ on the plate and so $\Gamma(s,t)$ takes the form

$$\Gamma(s,t) = \Gamma_-(t) + \int_{-1}^{s} \gamma(\lambda,t)\,\mathrm{d}\lambda, \tag{2.8}$$

where $\Gamma_-(t)$ can be considered a time-dependent constant of integration.

2.2. *The motion of the fluid*

To find expressions for $\gamma(s,t)$ and $\mu(s,t)$ it is necessary to introduce a more detailed description of the motion in the fluid surrounding the plate and so we introduce the complex-conjugate velocity field for the flow, denoted $\Phi(z,t) = u(z,t) - \mathrm{i}v(z,t)$ where $u(z,t)$ and $v(z,t)$ are the horizontal and vertical components of the fluid velocity at a general field point z. Since we are primarily concerned with information pertaining to the fluid motion on the upper and lower surfaces of the plate, we choose to write $\Phi(z,t)$ as a boundary integral of the form

$$\Phi(z,t) = \frac{1}{2\pi\mathrm{i}} \int_{-1}^{+1} \frac{\gamma(\lambda,t)\,\mathrm{d}\lambda}{(\zeta(\lambda,t) - z)} - \frac{1}{2\pi\mathrm{i}} \left[\int_0^{\Gamma_\pm(t)} \frac{\mathrm{d}\Lambda}{(\zeta_\pm(\Lambda,t) - z)} \right]_-^+, \tag{2.9}$$

where the square brackets again denote a difference such as $[\alpha_\pm]_-^+ = \alpha_+ - \alpha_-$. Inherent in the above Ansatz for $\Phi(z,t)$ are the following two assumptions. First, we have assumed that the falling plate can be successfully modelled as a bound vortex sheet whose position coincides with that of the plate. And second, we have assumed that the plate's wake can be successfully modelled as two trailing vortex sheets, each of which is shed from one of the plate's two sharp edges. The first term in equation (2.9) is the complex-conjugate velocity field induced by the bound vortex sheet and the remaining term represents the complex-conjugate velocity field induced by the two trailing vortex sheets. As a result, equation (2.9) is only able to represent flow fields in which the boundary layers on the plate separate tangentially at the edges $e_\pm(t)$. In other words, no secondary separation is permitted. However, the theoretical benefits associated with the use of equation (2.9) are compelling, as we will see.

The experienced reader will note that the two free vortex sheets have been parameterized using the circulation Γ – the complex number $\zeta_\pm(\Gamma,t)$ being used to denote the position of a point on one of the two trailing vortex sheets at which the circulation is Γ. See figure 2. This choice is convenient since it leads to the explicit appearance of $\Gamma_+(t)$ and $\Gamma_-(t)$ in equation (2.9), where $\Gamma_+(t)$ is the total circulation around the sheet that is shed from $e_+(t)$ and $\Gamma_-(t)$ is the negative of the total circulation around the sheet that is shed from $e_-(t)$. To simplify the forthcoming analysis, we will use the complex number $z_\pm(\Gamma,t)$ to denote the position of the point

$\zeta_\pm(\Gamma, t)$ as measured in the body frame of the plate. As a result, we write

$$z_\pm(\Gamma, t) = (\zeta_\pm(\Gamma, t) - c(t))e^{-i\theta(t)}. \tag{2.10}$$

Writing $\Phi(z, t)$ in the form (2.9) is also useful for a number of other reasons, not least of which is that $\Phi(z, t)$ then automatically satisfies the governing Euler equations as well as the proper far-field boundary conditions. Use of equation (2.9) also guarantees that the jump in the tangential component of the fluid velocity across the plate is $\gamma(s, t)$, as advertised in equation (2.7), and similarly guarantees that the circulation at $e_-(t)$ is $\Gamma_-(t)$, as advertised in equation (2.8). Furthermore, since $\Phi(z, t)$ must also satisfy Kelvin's circulation theorem, the kinematic boundary condition on the plate, and the unsteady Kutta condition, it can be shown that $\gamma(s, t)$ must take the form

$$\gamma(s, t) = \langle \gamma_\pm(t)a_\pm(s) \rangle_-^+ - \sqrt{1 - s^2}(2\dot\theta(t) + \langle b_\pm(s, t) \rangle_-^+), \tag{2.11}$$

where

$$\gamma_\pm(t) = \frac{1}{\partial_\Gamma z_\pm(\Gamma_\pm(t), t)}, \tag{2.12}$$

$$a_\pm(s) = 1 - \frac{1}{\pi} \arccos(\pm s), \tag{2.13}$$

$$b_\pm(s, t) = \frac{\gamma_\pm(t)a_\pm(s)}{\sqrt{1 - s^2}} \pm \frac{1}{\pi} \int_0^{\Gamma_\pm(t)} \mathrm{Re}\{\alpha(z_\pm(\Lambda, t), s)\}\mathrm{d}\Lambda, \tag{2.14}$$

and

$$\alpha(z, s) = \frac{1}{\sqrt{z + 1}\sqrt{z - 1}(z - s)}. \tag{2.15}$$

The reader is referred to Jones (2003) for a detailed derivation of this result. The angled brackets in equation (2.11) are used to denote a sum such as $\langle \alpha_\pm \rangle_-^+ = \alpha_+ + \alpha_-$ and it is important to note that both $a_\pm(s)$ and $b_\pm(s, t)$ are bounded functions of s, which approach well-defined limits as s approaches ± 1. In fact, $a_\pm(\pm 1) = 1$ and $a_\pm(\mp 1) = 0$ so that $\gamma(s, t)$ takes the values $\gamma_\pm(t)$ at $s = \pm 1$. As a result, it is clear from equations (2.9) and (2.11) that the complex-conjugate velocity field $\Phi(z, t)$ is bounded everywhere, in particular at each of plate's two sharp edges $z = e_\pm(t)$, and thus does indeed satisfy the unsteady Kutta condition. For completeness, we note that Kelvin's circulation theorem and the unsteady Kutta condition additionally require that $\Gamma_+(t)$ and $\Gamma_-(t)$ satisfy the two simultaneous integral constraints

$$-\frac{1}{\pi}\left[\int_0^{\Gamma_\pm(t)} \mathrm{Re}\left\{\frac{1}{\sqrt{z_\pm(\Lambda, t) + 1}\sqrt{z_\pm(\Lambda, t) - 1}}\right\}\mathrm{d}\Lambda\right]_-^+ = 2\nu(t), \tag{2.16}$$

$$-\frac{1}{\pi}\left[\int_0^{\Gamma_\pm(t)} \mathrm{Re}\left\{\frac{z_\pm(\Lambda, t)}{\sqrt{z_\pm(\Lambda, t) + 1}\sqrt{z_\pm(\Lambda, t) - 1}}\right\}\mathrm{d}\Lambda\right]_-^+ = \dot\theta(t), \tag{2.17}$$

where $\nu(t) = \mathrm{Im}\{\dot c(t)e^{-i\theta(t)}\}$ is the normal component of the velocity of the plate's centre of mass. However, we will consider the imposition of these constraints later on. Having imposed all the necessary boundary conditions, we can then use equation (2.9) to show that

$$\mu(s, t) = -\frac{1}{2\pi}\left[\int_0^{\Gamma_\pm(t)} \mathrm{Im}\left\{\frac{1}{(z_\pm(\Lambda, t) - s)}\right\}\mathrm{d}\Lambda\right]_-^+, \tag{2.18}$$

and then we have only to note that $\tau(t) = \mathrm{Re}\{\dot{c}(t)\mathrm{e}^{-\mathrm{i}\theta(t)}\}$ to complete our definitions of $\Gamma(s,t)$, $\gamma(s,t)$, $\mu(s,t)$, and $\tau(t)$. In principle, we can now reconstruct the pressure difference $[p_\pm(s,t)]^+_-$, the normal aerodynamic force $\mathbb{F}(t)$, and the aerodynamic torque $\mathbb{T}(t)$ using equations (2.7), (2.5), and (2.6).

At this point, it is useful to take a moment to consider how we have enlarged our description of the problem by choosing to describe the flow surrounding the plate using equations (2.9)–(2.18). In fact, we have introduced four new descriptive variables: $\zeta_+(\Gamma,t)$, $\zeta_-(\Gamma,t)$, $\Gamma_+(t)$, and $\Gamma_-(t)$. Together, these four variables completely describe the distribution of vorticity in the fluid surrounding the plate and in so doing completely characterize the dynamics of the plate's wake. See figure 2. Having identified our four new descriptive variables, we next consider their time evolution.

Fortunately, the problem of describing the time evolution of a free vortex sheet has already been considered by Birkhoff (1962) and Rott (1956), who solved the problem using a particularly elegant Lagrangian formulation. In this formulation the vortex sheet is parameterized using the circulation, as in the current formulation, and points on the sheet that conserve their circulation are shown to move with a velocity equal to the average of the fluid velocities on each side of the sheet. As a result, the boundary condition which states that the pressure should be continuous across the sheet is automatically satisfied. Application of these ideas to the problem under investigation leads to the differential equations

$$\partial_t \overline{\zeta}_\pm(\Gamma,t) = \varPhi(\zeta_\pm(\Gamma,t),t), \tag{2.19}$$

which govern the time evolution of the functions $\zeta_\pm(\Gamma,t)$ and, by definition, the dynamics of the wake. In addition, equations (2.19) must be supplemented by the ordinary differential equations

$$\dot{\Gamma}_\pm(t) = -\gamma_\pm(t)(\mu_\pm(t) - \tau(t)), \tag{2.20}$$

where $\mu_\pm(t) = \mu(\pm 1, t)$, which govern the time evolution of $\Gamma_\pm(t)$. Equations (2.20) result from the imposition of the integral constraints (2.16) and (2.17) in a time differentiated form. The formal details of the time differentiation are given in Jones (2003), but physically, equations (2.20) describe the rate at which circulation is shed from each of the plate's two sharp edges into the vortex wake. Equations (2.20) were also used by Krasny (1991) and Nitsche & Krasny (1994) in their work on the shedding of vorticity from the edges of flat plates and circular tubes.

Equations (2.1)–(2.20) then constitute a closed system of ordinary differential equations in the unknowns $c(t)$, $\theta(t)$, $\dot{c}(t)$, $\dot{\theta}(t)$, $\zeta_\pm(\Gamma,t)$, and $\Gamma_\pm(t)$, which can be integrated forward in time to find the trajectory of the falling plate and the resulting motion in the surrounding fluid. However, before seeking a solution to equations (2.1)–(2.20), numerical or otherwise, it is essential that we understand their structure in more detail. In particular, we must first determine whether the governing evolution equations – equations (2.3), (2.4), (2.19), and (2.20) – are explicit in the unknowns $c(t)$, $\theta(t)$, $\dot{c}(t)$, $\dot{\theta}(t)$, $\zeta_\pm(\Gamma,t)$, and $\Gamma_\pm(t)$.

2.3. *The interaction between the plate and the fluid*

It is relatively straightforward to see that the differential equations (2.19) and (2.20) are explicit in the unknowns $c(t)$, $\theta(t)$, $\dot{c}(t)$, $\dot{\theta}(t)$, $\zeta_\pm(\Gamma,t)$, and $\Gamma_\pm(t)$, since the functions $\gamma(s,t)$ and $\mu(s,t)$ are themselves explicit in those unknowns according to equations (2.11)–(2.18). However, it is not so easy to see whether equations (2.3) and (2.4) are similarly explicit or not. This is solely due to the appearance of the time derivative $\partial_t \Gamma(s,t)$ on the right-hand side of equation (2.7) and so we must next examine this

term in more detail. We begin by differentiating equation (2.8) with respect to time while holding s fixed to obtain

$$\partial_t \Gamma(s, t) = \dot{\Gamma}_-(t) + \int_{-1}^{s} \partial_t \gamma(\lambda, t) \, d\lambda, \tag{2.21}$$

where $\dot{\Gamma}_-(t)$ is as defined in equation (2.20) and

$$\partial_t \gamma(s, t) = \langle \dot{\gamma}_\pm(t) a_\pm(s) \rangle_-^+ - \sqrt{1-s^2}(2\ddot{\theta}(t) + \langle \partial_t b_\pm(s, t) \rangle_-^+). \tag{2.22}$$

We continue by investigating the time derivatives $\dot{\gamma}_\pm(t)$ and $\partial_t b_\pm(s, t)$. By differentiating equation (2.14) we obtain the latter term in the form

$$\partial_t b_\pm(s, t) = \frac{\dot{\gamma}_\pm(t) a_\pm(s)}{\sqrt{1-s^2}} \pm \frac{1}{\pi} \partial_t \int_0^{\Gamma_\pm(t)} \text{Re}\left\{\alpha(z_\pm(\Lambda, t), s)\right\} d\Lambda. \tag{2.23}$$

Before differentiating the integral in equation (2.23) with respect to time, it is important to note that the integrand $\alpha(z, t)$ has an inverse square-root singularity at the upper limit of integration since $z_\pm(\Gamma_\pm(t), t) = \pm 1$. As a result, it is helpful to rewrite the integral in the form

$$\lim_{\varepsilon \to 0} \partial_t \int_0^{\Gamma_\pm(t)-\varepsilon} \text{Re}\left\{\alpha(z_\pm(\Lambda, t), s)\right\} d\Lambda,$$

thereby temporarily avoiding the problems associated with the singularity. The time derivative can then be performed without incident using the formula for the derivative of an integral with a variable limit of integration, and subsequent use of integration by parts in the resulting expression, followed by the evaluation of the limit $\varepsilon \to 0$ using equations (2.12), (2.15), and (2.18)–(2.20), then leads to the result

$$\partial_t \int_0^{\Gamma_\pm(t)} \text{Re}\left\{\alpha(z_\pm(\Lambda, t), s)\right\} d\Lambda = \eta_\pm(s, t) + \int_0^{\Gamma_\pm(t)} \text{Re}\left\{\alpha(z_\pm(\Lambda, t), s)\partial_\Gamma \beta_\pm(\Lambda, t)\right\} d\Lambda,$$

where $\eta_\pm(s, t) = \text{Re}\{\alpha(z_\pm(0, t), s)\beta_\pm(0, t)\}$ and $\beta_\pm(\Gamma, t) = -\partial_t z_\pm(\Gamma, t)/\partial_\Gamma z_\pm(\Gamma, t)$. Furthermore, since equation (2.23) must remain bounded at $s = \pm 1$, the above result can be used to show that $\dot{\gamma}_\pm(t)$ take the form

$$\dot{\gamma}_\pm(t) = -\gamma_\pm(t)\text{Re}\{\partial_\Gamma \beta_\pm(\Gamma_\pm(t), t)\}. \tag{2.24}$$

Since both $\alpha(z_\pm(\Gamma, t), s)$ and $\beta_\pm(\Gamma, t)$ are explicit in the unknowns $c(t)$, $\theta(t)$, $\dot{c}(t)$, $\dot{\theta}(t)$, $\zeta_\pm(\Gamma, t)$, and $\Gamma_\pm(t)$ it is now clear that equation (2.23) is similarly explicit. Unfortunately, the appearance of $\ddot{\theta}(t)$ in equation (2.22) implies that $\mathbb{F}(t)$ and $\mathbb{T}(t)$ depend on $\ddot{\theta}(t)$ through equations (2.5)–(2.7) and (2.21)–(2.23). As a result, the equations of motion (2.3) and (2.4) are implicit in $\ddot{c}(t)$ and $\ddot{\theta}(t)$. The implicit nature of the governing equations should not surprise us because it reflects the interactive nature of the problem in hand. However, it is rather unusual and therefore worthy of note.

Finally, we note that the equations of motion (2.3) and (2.4) are also linear in $\ddot{c}(t)$ and $\ddot{\theta}(t)$ and as such can be solved straightforwardly to obtain an explicit set of governing equations as required.

3. Asymptotic small-time solution

In general, the falling plate is released from rest and so the question of how the free vortex sheets come into existence is an important one. We can answer this question by constructing a small-time asymptotic solution to the system of equations (2.1)–(2.20).

Just after the plate is released we expect the solution to consist of two small starting vortices, one at each of the plate's two sharp edges, which take the form of two infinite spiral vortex sheets. See the theoretical and experimental work of Moore (1974, 1975), Pullin (1978), Pullin & Perry (1980), and Pullin & Wang (2004). For small enough times $t > 0$, these spiral vortex sheets are expected to have approximately self-similar structure in time due to the absence of a typical length scale in the regions surrounding the edges. With this in mind it is possible to show, using scaling arguments, that equations (2.1)–(2.20) admit asymptotically self-similar solutions of the form

$$c(t) \sim c_0 + \alpha_0 e^{i\vartheta_0} t^{m+1} + \cdots, \tag{3.1}$$

$$\theta(t) \sim \theta_0 + \beta_0 t^{m+1} + \cdots, \tag{3.2}$$

$$\zeta_\pm(\Gamma, t) \sim c_\pm(t) \pm |\delta_\pm|^{2/3} t^{2(m+1)/3} \omega_\pm(\tau_\pm(\Gamma, t)) e^{i\theta(t)} + \cdots, \tag{3.3}$$

$$\Gamma_\pm(t) \sim J_\pm |\delta_\pm|^{4/3} t^{(4m+1)/3} + \cdots, \tag{3.4}$$

where the similarity variables $\tau_\pm(\Gamma, t)$ are defined to be

$$\tau_\pm(\Gamma, t) = 1 - \Gamma J_\pm^{-1} |\delta_\pm|^{-4/3} t^{-(4m+1)/3}. \tag{3.5}$$

As in Jones (2003), the functions $\omega_\pm(\tau_\pm)$ then satisfy the integro-differential equations

$$p\,\overline{\omega}_\pm(\tau_\pm) + q(1 - \tau_\pm)\overline{\omega}'_\pm(\tau_\pm) = \mp \frac{J_\pm}{2\pi i} \left[\int_0^1 \frac{d\tau}{\omega_\pm(\tau) - \omega_\pm(\tau_\pm)} + \int_{-\infty}^0 \frac{\sqrt{-\xi}\,F_\pm(\xi)}{(\xi - \omega_\pm(\tau_\pm))} d\xi \right], \tag{3.6}$$

where $p = 2(m+1)/3$, $q = (4m+1)/3$, and

$$F_\pm(\xi) = \frac{1}{\pi} \int_0^1 \mathrm{Re}\left\{ \frac{1}{\sqrt{\omega_\pm(\tau)}(\omega_\pm(\tau) - \xi)} \right\} d\tau, \tag{3.7}$$

The boundary conditions $\omega_\pm(0) = 0$ and $\mathrm{Im}\{\omega'_\pm(0)\} = 0$, which ensure that the spiral vortex sheets join up with the edges of the plate and separate tangentially, must also be satisfied. The unknown constants $\delta_\pm$ and $J_\pm$ can be shown to take the values

$$\delta_\pm = \alpha_0 \sin(\vartheta_0 - \theta_0) \pm \frac{\beta_0}{2}, \tag{3.8}$$

$$J_\pm = -\sqrt{2}\,\pi(m+1)\,\mathrm{sgn}\delta_\pm \left[\int_0^1 \mathrm{Re}\left\{ \frac{1}{\sqrt{\omega_\pm(\tau)}} \right\} d\tau \right]^{-1}. \tag{3.9}$$

However, in contrast with the cases considered by Jones (2003), the constants m, α_0, ϑ_0, and β_0 are also unknown and must be determined as part of the solution. In fact, if we assume that the prescribed force and torque, $F(t)$ and $T(t)$, have the small-time asymptotic expansions

$$F(t) \sim F_0 t^{n-1} + \cdots, \tag{3.10}$$

$$T(t) \sim T_0 t^{n-1} + \cdots, \tag{3.11}$$

then substitution of the asymptotic expansions (3.1)–(3.4) into equations (2.3) and (2.4) – the governing equations of motion for the falling plate – followed by the series expansion of the resulting expressions in powers of t using equations (A 1)–(A 10) in
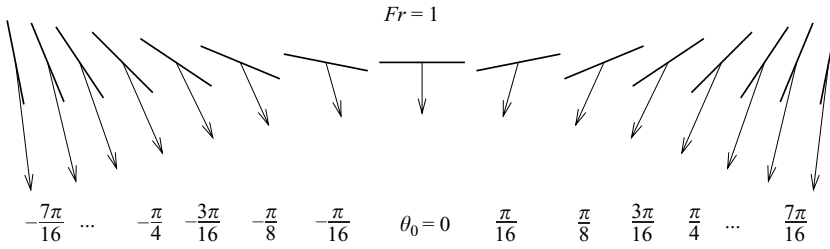
$Fr = 1$

$$-\frac{7\pi}{16} \quad \cdots \quad -\frac{\pi}{4} \quad -\frac{3\pi}{16} \quad -\frac{\pi}{8} \quad -\frac{\pi}{16} \quad \theta_0 = 0 \quad \frac{\pi}{16} \quad \frac{\pi}{8} \quad \frac{3\pi}{16} \quad \frac{\pi}{4} \quad \cdots \quad \frac{7\pi}{16}$$

FIGURE 3. The initial force vector on a falling plate after release from rest at modified Froude number $Fr = 1$. The vectors shown represent the initial force on the plate's centre of mass (normalized so that the magnitude of the longest vector is 3) for the initial angles $\theta_0 = -7\pi/16$, $-3\pi/8$, $-5\pi/16$, ..., $5\pi/16$, $3\pi/8$, and $7\pi/16$.

the Appendix, shows that

$$m = n, \tag{3.12}$$

and that the constants α_0, ϑ_0, and β_0 can be expressed in the form

$$\alpha_0 e^{i\vartheta_0} = \frac{1}{n(n+1)Fr}\left[F_0 - \frac{\pi}{(\pi + 2Fr)}\mathrm{Im}\left\{F_0 e^{-i\theta_0}\right\}ie^{i\theta_0}\right], \tag{3.13}$$

$$\beta_0 = \frac{3}{n(n+1)Fr}\left[T_0 - \frac{3\pi}{(3\pi + 16Fr)}T_0\right], \tag{3.14}$$

where terms of higher order than $O(t^{m-1})$ have been neglected.

Within the context of the falling card problem ($n = 1$, $F_0 = -i$, and $T_0 = 0$), the above result shows that the centre of mass of the plate does not fall vertically downward immediately after its release, as one might expect, but instead slides sideways and down along a straight line, the slope of which depends on the initial angle θ_0 and the modified Froude number Fr. This observation is significant since it shows that the aerodynamic response to the downward pull of gravity is immediate and does not take time to build up. However, the response is produced by nothing more than the acceleration reaction of the fluid (see Batchelor 1967, p. 405); the unsteady forces that arise from the continual shedding of vorticity enter only at $O(t^{2(2m-1)/3})$. In any case, the effective sideways and downward forces on the plate at release take the form

$$Fr\,\mathrm{Re}\{\ddot{c}(0)\} = -\frac{\pi}{2(\pi + 2Fr)}\sin 2\theta_0, \tag{3.15}$$

$$Fr\,\mathrm{Im}\{\ddot{c}(0)\} = \frac{\pi}{(\pi + 2Fr)}\cos^2\theta_0 - 1. \tag{3.16}$$

A graphical illustration of the force vectors at $Fr = 1$ and for a range of initial angles θ_0 is presented in figure 3.

To complete our description of the asymptotic small-time solution it is necessary to find $\omega_\pm(\tau_\pm)$ by solving the integro-differential equations (3.6) subject to the boundary conditions $\omega_\pm(0) = 0$ and $\mathrm{Im}\{\omega'_\pm(0)\} = 0$. This was done numerically, for $m = 1$, using a method not unlike that employed by Pullin (1978) and the real and imaginary parts of the resulting solution, as well as the parametric spiral solution, are plotted in figure 4.
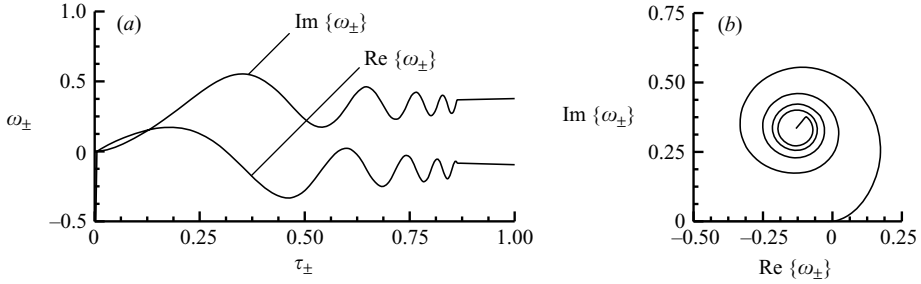
FIGURE 4. The solution for $\omega_{\pm}(\tau_{\pm})$; (a) the real and imaginary parts of $\omega_{\pm}(\tau_{\pm})$ plotted against the similarity variable $\tau_{\pm}$; (b) a parametric plot of the self-similar spiral vortex sheet. In the case pictured above $J_{\pm} \approx -6.4352$.

4. Numerical solution

Having explored the small-time solution of equations (2.1)–(2.20) asymptotically we next seek the solution at larger times and therefore resort to a numerical approach. The numerical method employed here is similar to that used in Jones (2003) and the reader is referred to that study for a detailed description of the algorithm used. However, some modification of the numerical method was necessary in order to incorporate the interactive nature of the present problem, and so the method is re-presented here in brief.

To begin with, we note that the evolution equations for $\zeta_{\pm}(\Gamma, t)$ are ill-posed and lead generically to weak curvature singularities as discovered by Moore (1979) and later investigated by Krasny (1986b), Shelley (1992), and others. As a result, finding a solution at long times requires regularization; see the work of Krasny (1986a, b), and Baker & Shelley (1990). Accordingly, we follow Krasny (1986a) and modify equation (2.19) by replacing the Cauchy kernel therein with the vortex-blob kernel

$$K_{\delta}(z) = \frac{\overline{z}}{|z|^2 + \delta^2}, \tag{4.1}$$

where δ is a small positive constant. Since $K_{\delta}(z)$ approaches the Cauchy kernel as $\delta \to 0$ it is hoped that the solution of the resulting system of ordinary differential equations will converge to the physically relevant solution as $\delta \to 0$. Indeed, Liu & Xin (1995) have already proven that a class of vortex-blob methods converge to weak solutions of the two-dimensional Euler equations as $\delta \to 0$ under certain assumptions. A consistent treatment of the problem then demands that similar modifications be made to equations (2.9)–(2.20). However, we will not concern ourselves with the details of the modifications here. For our purposes, it is sufficient to note that the expressions for the aerodynamic forces and torques, reproduced in the Appendix, remain formally unchanged under this substitution, the only difference being that the kernels $\delta_n(z)$ become slightly modified.

4.1. Time-marching algorithm

Having accepted these modifications, we continue by partitioning the time interval over which the solution is required into a number of small sub-intervals that are separated by the discrete times t_i, where $i = 1, \ldots, I$ and $t_0 = 0$. At time t_i, the position of the plate's centre of mass is denoted using the complex number c_i and the
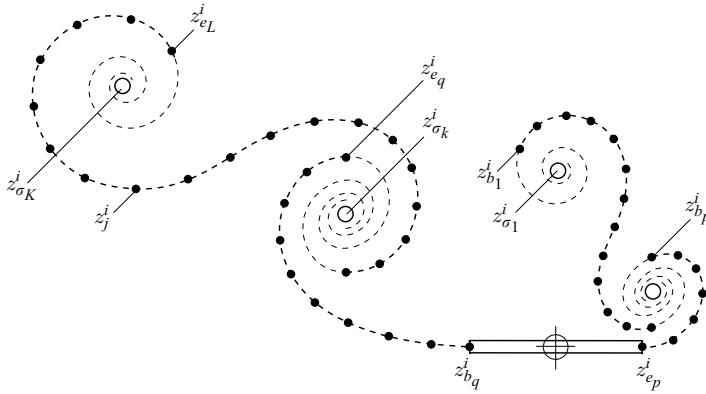
FIGURE 5. The discretized vortex wake in the body frame. The trailing vortex sheets are discretized using J Lagrangian vortex blobs (•), any tightly wound spiral portions being replaced with a point vortex at the spiral centre (∘). In total, there are K point vortices and L vortex blob sheets.

angle between the plate and the horizontal is similarly denoted using the real number θ_i. The two trailing vortex sheets are then discretized using a total of J Lagrangian points whose positions, relative to the plate, are denoted using the complex numbers z_j^i for $j = 1, \ldots, J$. Likewise, the circulation at each Lagrangian point is denoted using the real numbers Γ_j^i for $j = 1, \ldots, J$. The integer j is referred to as the Lagrangian index of the point z_j^i. Since z_j^i denotes only the relative position of each Lagrangian point, the actual position can be reconstructed from c_i, θ_i, and z_j^i in the form $\zeta_j^i = c_i + z_j^i e^{i\theta_i}$ if required.

Having discretized the solution, we next take our approximation a step further by replacing the inner turns of any tightly wound spiral portions of the free vortex sheets with K isolated point vortices; one point vortex at each spiral centre. See figure 5. To keep track of these point vortices, we denote their Lagrangian indices using the integers σ_k for $k = 1, \ldots, K$. For convenience, we also denote the Lagrangian indices of the beginning and end of the intervening vortex sheet segments using the integers b_ℓ and e_ℓ, for $\ell = 1, \ldots, L$, the Lagrangian indices of the plate's edges $e_+ (t_i)$ and $e_- (t_i)$ being denoted e_p and b_q. At this point, the wake therefore consists of K isolated point vortices surrounded by a collection of L disjoint vortex sheet segments, two of which are being shed continuously from the edges $z_{e_p}^i$ and $z_{b_q}^i$.

It is next necessary to develop an algorithm that approximates the unknown time derivatives $\ddot{c}_i$, $\ddot{\theta}_i$, and $\dot{z}_j^i$ and $\dot{\Gamma}_j^i$ for $j = 1, \ldots, J$ in terms of the known quantities c_i, $\dot{c}_i$, θ_i, $\dot{\theta}_i$, and z_j^i and Γ_j^i for $j = 1, \ldots, J$. If we had such an algorithm, the resulting time derivatives could then be used as part of a Runge–Kutta scheme to produce corresponding approximations for the unknowns c_{i+1}, $\dot{c}_{i+1}$, θ_{i+1}, $\dot{\theta}_{i+1}$, and z_j^{i+1} and Γ_j^{i+1} for $j = 1, \ldots, J$; thus the solution could be marched forward in time. To begin with, we choose to approximate $\ddot{c}_i$ and $\ddot{\theta}_i$ using

$$Fr\, \ddot{c}_i = F(t_i) + \tfrac{1}{2} \left(\mathbb{F}_s + \mathbb{F}_u + \mathbb{F}_w \right) i e^{i\theta_i}, \tag{4.2}$$

$$\tfrac{1}{3} Fr\, \ddot{\theta}_i = T(t_i) + \tfrac{1}{2} \left(\mathbb{T}_s + \mathbb{T}_u + \mathbb{T}_w \right), \tag{4.3}$$

where the steady normal force and torque are approximated in the form

$$\mathbb{F}_s = -\text{Re}\left\{ \dot{c}_i e^{-i\theta_i} \right\} \left(\Gamma_{e_p}^i - \Gamma_{b_q}^i \right), \tag{4.4}$$

$$\mathbb{T}_s = -\pi \operatorname{Re} \left\{ \dot{c}_i \mathrm{e}^{-\mathrm{i}\theta_i} \right\} \operatorname{Im} \left\{ \dot{c}_i \mathrm{e}^{-\mathrm{i}\theta_i} \right\}, \tag{4.5}$$

the unsteady normal force and torque are approximated in the form

$$\mathbb{F}_u = \dot{\Gamma}^i_{e_p} + \dot{\Gamma}^i_{b_q} - \tfrac{\pi}{2} \dot{\alpha}_2, \tag{4.6}$$

$$\mathbb{T}_u = \tfrac{3}{8} \left(\dot{\Gamma}^i_{e_p} - \dot{\Gamma}^i_{b_q} \right) - \tfrac{\pi}{8} \dot{\alpha}_3, \tag{4.7}$$

and the wake-induced normal force and torque are approximated in the form

$$\mathbb{F}_w = \frac{1}{2}(\beta_0 - \beta_2)\left(\Gamma^i_{e_p} - \Gamma^i_{b_q}\right) + \frac{\pi}{2} \sum_{n=2}^{N-1} \alpha_n \left(\beta_{n-1} - \beta_{n+1}\right), \tag{4.8}$$

$$\mathbb{T}_w = \frac{1}{4}(\beta_1 - \beta_3)\left(\Gamma^i_{e_p} - \Gamma^i_{b_q}\right) + \frac{\pi}{2}(\alpha_0 - \alpha_2) \operatorname{Re}\left\{\dot{c}_i \mathrm{e}^{-\mathrm{i}\theta_i}\right\} + \frac{\pi}{4} \sum_{n=2}^{N-2} \alpha_n \left(\beta_{n-2} - \beta_{n+2}\right). \tag{4.9}$$

The approximations outlined above follow straightforwardly from the exact expressions for the normal force and torque on a moving flat plate as derived in Jones (2003). The relevant expressions are reproduced in the Appendix for convenience. We continue by approximating the complex conjugate of $\dot{z}^i_j$ in the form

$$\overline{\dot{z}^i_j} = \frac{\mathrm{i}}{2\pi} \left[\sum_{\substack{k=1 \\ \sigma_k \neq j}}^{K} \frac{w_{\sigma_k}}{\left(z^i_{\sigma_k} - z^i_j\right)} + \frac{1}{2} \sum_{\ell=1}^{L} \sum_{m=b_\ell}^{e_\ell} w_m K_\delta \left(z^i_m - z^i_j\right) + 2\pi \sum_{n=1}^{N} \alpha_n \, \varepsilon_n \left(z^i_j\right) \right] - \overline{\Omega}\left(z^i_j\right), \tag{4.10}$$

for $j = 1, \ldots, J$. The above approximation is a discrete and desingularized version of the Birkhoff–Rott equation (2.19), in which the wake integrals have been approximated using a simple quadrature formula and where $\gamma(s, t)$ has been expanded in the form of a truncated Chebyshev series of the second kind, the remaining spatial integration having been performed exactly. As a result, the real weights w_j take the form

$$w_j = \begin{cases} \Gamma_{j+1} - \Gamma_{j-1} & \text{for} \quad j = \sigma_k \quad k = 1, \ldots, K \\ \Gamma_{j+1} - \Gamma_j & \text{for} \quad j = b_\ell \quad \ell = 1, \ldots, L \\ \Gamma_{j+1} - \Gamma_{j-1} & \text{for} \quad j = b_\ell + 1, \ldots, e_\ell - 1 \quad \ell = 1, \ldots, L \\ \Gamma_j - \Gamma_{j-1} & \text{for} \quad j = e_\ell \quad \ell = 1, \ldots, L, \end{cases} \tag{4.11}$$

and the basis functions $\varepsilon_n(z)$ take the form $\varepsilon_n(z) = (z - \sqrt{z+1}\sqrt{z-1})^n$. Additionally, $\Omega(z) = \dot{c}_i \mathrm{e}^{-\mathrm{i}\theta_i} + \mathrm{i}\dot{\theta}_i(z - \overline{\varepsilon_1}(z))$. At this point, the observant reader will note that equations (4.4)–(4.10) all depend on the, as yet unknown, coefficients α_n and β_n for $n = 0 \ldots, N$ and we must next develop approximations for these coefficients. Fortunately, α_n and β_n can be expressed in the form

$$\alpha_n + \mathrm{i}\beta_n = \frac{2}{N}\left[\frac{1}{2}\psi_0 + \sum_{m=1}^{N-1} \psi_m \cos\left(\frac{\pi m n}{N}\right) + \frac{1}{2}(-1)^n \, \psi_N \right], \tag{4.12}$$

for $n = 0, \ldots, N$, which can be efficiently evaluated using the discrete cosine transform algorithm. In essence, the above relationship ensures that the no-penetration boundary condition is satisfied at the points $\zeta(s_n, t)$ for $n = 0, \ldots, N$ where $s_n = \cos(\pi n / N)$.

For this to be the case, the interpolated values ψ_n must also take the form

$$\psi_n = -\frac{1}{2\pi}\left[\sum_{k=1}^{K}\frac{w_{\sigma_k}}{\left(z_{\sigma_k}^i - s_n\right)} + \frac{1}{2}\sum_{\ell=1}^{L}\sum_{j=b_\ell}^{e_\ell} w_j K_\delta\left(z_j^i - s_n\right)\right], \tag{4.13}$$

for $n = 0, \ldots, N$. At this point, it would appear that we are in a position to evaluate the coefficients α_n and β_n for $n = 0, \ldots, N$. However, we are not. We have yet to satisfy the additional constraints

$$\alpha_0 = 2\,\text{Im}\{\dot{c}_i e^{-i\theta_i}\}, \tag{4.14}$$

$$\alpha_1 = \dot{\theta}_i + \frac{1}{\pi}\left(\Gamma_{e_p}^i - \Gamma_{b_q}^i\right), \tag{4.15}$$

which are the discrete versions of simultaneous integral constraints (2.16) and (2.17). Since both α_0 and α_1 are themselves linear functions of $\Gamma_{e_p}^i$ and $\Gamma_{b_q}^i$, as can be verified by substituting equations (4.11) and (4.13) into equation (4.12), the constraints (4.14) and (4.15) represent two simultaneous linear equations for $\Gamma_{e_p}^i$ and $\Gamma_{b_q}^i$ and, as such, can be solved exactly; simple Gaussian elimination is used in practice. Having found $\Gamma_{e_p}^i$ and $\Gamma_{b_q}^i$, and having re-computed the dependent variables w_{e_p-1}, w_{e_p}, w_{b_q}, w_{b_q+1}, ψ_n, α_n, and β_n for $n = 0, \ldots, N$, it is then possible to evaluate the velocities $\dot{z}_j^i$ for $j = 1, \ldots, J$ using equation (4.10). Note that it is also possible to evaluate $\mathbb{F}_s$, $\mathbb{T}_s$, $\mathbb{F}_w$, and $\mathbb{T}_w$ at this stage.

In the current interactive context it is also necessary to evaluate the unsteady loads $\mathbb{F}_u$ and $\mathbb{T}_u$ and these loads depend on the time derivatives $\dot{\Gamma}_{e_p}^i$, $\dot{\Gamma}_{b_q}^i$, and $\dot{\alpha}_n$ for $n = 0, \ldots, N$. We therefore differentiate equation (4.12) with respect to time and write

$$\dot{\alpha}_n + i\dot{\beta}_n = \frac{2}{N}\left[\frac{1}{2}\dot{\psi}_0 + \sum_{m=1}^{N-1}\dot{\psi}_m\cos\left(\frac{\pi mn}{N}\right) + \frac{1}{2}(-1)^n\,\dot{\psi}_N\right], \tag{4.16}$$

for $n = 0, \ldots, N$, where

$$\dot{\psi}_n = \frac{1}{2\pi}\left[\sum_{k=1}^{K}\frac{w_{\sigma_k}\dot{z}_{\sigma_k}^i}{\left(z_{\sigma_k}^i - s_n\right)^2} - \frac{1}{2}\sum_{\ell=1}^{L}\sum_{j=b_\ell}^{e_\ell} w_j L_\delta\left(z_j^i - s_n, \dot{z}_j^i\right)\right] + \dot{\Gamma}_{e_p}^i\frac{\partial\psi_n}{\partial\Gamma_{e_p}^i} + \dot{\Gamma}_{b_q}^i\frac{\partial\psi_n}{\partial\Gamma_{b_q}^i}, \tag{4.17}$$

for $n = 0, \ldots, N$. In equation (4.17) the kernel $L_\delta(z, \dot{z})$ is the full time derivative of the vortex-blob kernel $K_\delta(z)$ and, as such, takes the form

$$L_\delta(z, \dot{z}) = \frac{\bar{\dot{z}} - 2K_\delta(z)\text{Re}\{\bar{z}\dot{z}\}}{|z|^2 + \delta^2}. \tag{4.18}$$

Again, we seem to be in a position to evaluate the coefficients $\dot{\alpha}_n$ and $\dot{\beta}_n$ for $n = 0, \ldots, N$, but we are not; $\dot{\Gamma}_{e_p}^i$ and $\dot{\Gamma}_{b_q}^i$ must first satisfy the time-differentiated constraints

$$\dot{\alpha}_0 = 2\,\text{Im}\{(\ddot{c}_i - i\dot{c}_i\dot{\theta}_i)e^{-i\theta_i}\}, \tag{4.19}$$

$$\dot{\alpha}_1 = \ddot{\theta}_i + \frac{1}{\pi}\left(\dot{\Gamma}_{e_p}^i - \dot{\Gamma}_{b_q}^i\right), \tag{4.20}$$

Since the time derivatives $\ddot{c}_i$ and $\ddot{\theta}_i$ are linearly dependent on $\dot{\Gamma}_{e_p}^i$ and $\dot{\Gamma}_{b_q}^i$, through equations (4.2), (4.3), (4.6), and (4.7), and the coefficients $\dot{\alpha}_0$ and $\dot{\alpha}_1$ are linearly

dependent on $\dot{\Gamma}^i_{e_p}$ and $\dot{\Gamma}^i_{b_q}$, through equations (4.16) and (4.17), the equations (4.19) and (4.20) are two simultaneous linear equations in $\dot{\Gamma}^i_{e_p}$ and $\dot{\Gamma}^i_{b_q}$ and, as such, can be solved exactly. Again, Gaussian elimination is used in practice and the dependent variables $\mathbb{F}_u$, $\mathbb{T}_u$, $\ddot{c}_i$, $\ddot{\theta}_i$, $\dot{\psi}_n$, $\dot{\alpha}_n$, and $\dot{\beta}_n$ for $n = 0, \ldots, N$ are re-computed as part of the algorithm.

Finally, since the circulation is a Lagrangian variable, we note that $\dot{\Gamma}^i_j = 0$ for all remaining values of j and so the desired time derivatives $\ddot{c}_i$, $\ddot{\theta}_i$, and $\dot{z}^i_j$ and $\dot{\Gamma}^i_j$ are then available for $j = 1, \ldots, J$.

4.2. *Initial conditions*

In order to initialize our solution, the values of c_1, θ_1, $\dot{c}_1$, $\dot{\theta}_1$, Γ^1_j, and z^1_j for $j = 1, \ldots, J$ are required. These values are provided using a simplified version of the small-time solution outlined in §3. First, we set $J = 4$, $K = 2$, $\sigma_1 = 1$, $\sigma_K = 4$, $L = 2$, $p = 1$, $q = 2$, $b_p = e_p = 2$, and $b_q = e_q = 3$. Next, we compute the constants $\delta_\pm$, m, $\alpha_0 e^{i\vartheta_0}$, β_0, $K_\pm = -2\pi(m+1)(3/8)^{1/3}\,\mathrm{sgn}\delta_\pm$, and $\Omega_\pm = \mp i(3/8)^{2/3}\,\mathrm{sgn}\delta_\pm$ (according to their definitions in §3) for arbitrary n, θ_0, c_0, F_0, T_0, and Fr. Having done this, we choose an initial time $t_1 > 0$ and define the initial position and velocity of the plate to be

$$c_1 = c_0 + \alpha_0 e^{i\vartheta_0} t_1^{m+1}, \qquad (4.21)$$

$$\theta_1 = \theta_0 + \beta_0 t_1^{m+1}, \qquad (4.22)$$

$$\dot{c}_1 = (m+1)\alpha_0 e^{i\vartheta_0} t_1^m, \qquad (4.23)$$

$$\dot{\theta}_1 = (m+1)\beta_0 t_1^m. \qquad (4.24)$$

We define the initial circulation distribution to be

$$\Gamma^1_1 = 0, \qquad (4.25)$$

$$\Gamma^1_{e_p} = K_+ |\delta_+|^{4/3} t_1^{(4m+1)/3}, \qquad (4.26)$$

$$\Gamma^1_{b_q} = K_- |\delta_-|^{4/3} t_1^{(4m+1)/3}, \qquad (4.27)$$

$$\Gamma^1_J = 0, \qquad (4.28)$$

and the initial wake configuration to be

$$z^1_1 = 1 + \Omega_+ |\delta_+|^{2/3} t_1^{2(m+1)/3}, \qquad (4.29)$$

$$z^1_{e_p} = 1, \qquad (4.30)$$

$$z^1_{b_q} = -1, \qquad (4.31)$$

$$z^1_J = -1 - \Omega_- |\delta_-|^{2/3} t_1^{2(m+1)/3}. \qquad (4.32)$$

This initial solution is then marched forward in time using the algorithm previously described. During the calculation, additional Lagrangian points are introduced into the calculation at each of the plate's two sharp edges (one at each edge at the beginning of each time step) to model the continual shedding of vorticity from those edges. Others are inserted adaptively to accurately represent the evolving shape of the free vortex sheets; Lagrangian points are also deleted in places where they are no longer required. The details of these surgical procedures are not included here, but the reader is referred to preparatory study of Jones (2003) for a detailed account of the algorithms used.

4.3. *Limitations of the numerical method*

Having described the numerical method used, we next highlight its practical limitations. Most notably, the method only makes physical sense if

$$\mu_+(t) - \tau(t) > 0 \quad \text{and} \quad \mu_-(t) - \tau(t) < 0. \tag{4.33}$$

These conditions together ensure that any newly shed Lagrangian particles move away from (instead of onto) each of the plate's two sharp edges. Unfortunately, these conditions seem not always to hold in situations of current and practical interest and no algorithm has yet been proposed to deal with such circumstances adequately. As a result, the method used here is only able to compute the solution while the logical statement in equation (4.33) holds true. In practical terms this restricts our investigation to high effective angles of incidence, a situation which, due to the interactive nature of the problem, tends to prevail at the higher modified Froude numbers.

Another drawback of the method is that it requires $O(J^2)$ floating point operations per time step, where J is the total number of Lagrangian points in the calculation. In practice, this means that the method becomes prohibitively expensive when the complexity of the solution demands the use of tens of thousands of Lagrangian points. However, the fast summation methods of Greengard & Rokhlin (1987) and Draghicescu & Draghicescu (1995) can be used to compute the sums appearing in equation (4.10) in $O(J)$ flops per time step. Another option is to use the simpler tree-code algorithms of Lindsay & Krasny (2001), which reduce the operation count to $O(J \log J)$.

5. Results and discussion

We now present a number of numerical solutions to the full system of governing equations (2.1)–(2.20), each of which is an approximate solution of the falling card problem. The external forcing is provided by the constant downward pull of gravity and so $F(t) = -i$ and $T(t) = 0$. In general, the plate is released from rest with an initial angle of inclination θ_0. Its subsequent motion, together with the resulting motion in the surrounding fluid, is then computed, as long as the logical statement in equation (4.33) is true.

A number of solutions are presented in figures 6–18 at the modified Froude numbers $Fr = 1, 2,$ and 4 and for the initial inclinations $\theta_0 = 0, \pi/1024, \pi/512, \pi/256, \pi/128, \pi/64,$ and $\pi/32$. These parameter ranges essentially characterize the scope of the current numerical method; computations at $Fr < 1$ or for $\theta_0 > \pi/32$ are severely restricted by equation (4.33). Unless otherwise stated, the solution was computed at the discrete times $t_0 = 0$, $t_1 = 1/16$, $t_2 = 5/64$, $t_3 = 6/64$, $t_4 = 7/64$, etc., using the algorithm described in §4 with $\delta = 0.2$ and $N = 128$. Direct summation was used to compute the sums in equations (4.10), (4.13), and (4.17) and a fourth-order Runge–Kutta method was used to do the time stepping.

Figure 6 shows the trajectory of the falling plate for each of the twenty-one parameter combinations considered. Each plot is a collage of frames showing the plate's position at the times $t = 0, 0.5, 1, 1.5, 2,$ etc. A subset of these computations are represented in more detail in figures 7–16. This subset of computations is labelled (a)–(j) and the corresponding plate trajectories are identified in figure 6. Figures 7, 8, and 9 describe the dynamics of the falling plate by plotting the real and imaginary parts of the functions $c(t)$, $\dot{c}(t)$, and $\ddot{c}(t)$, and the functions $\theta(t)$, $\dot{\theta}(t)$, and $\ddot{\theta}(t)$ against time. Figures 10, 11, and 12 show the evolution of the trailing vortex wake for examples (a)–(i) for $Fr = 1, 2,$ and 4 and $\theta_0 = 0, \pi/1024,$ and $\pi/256$. In each plot the
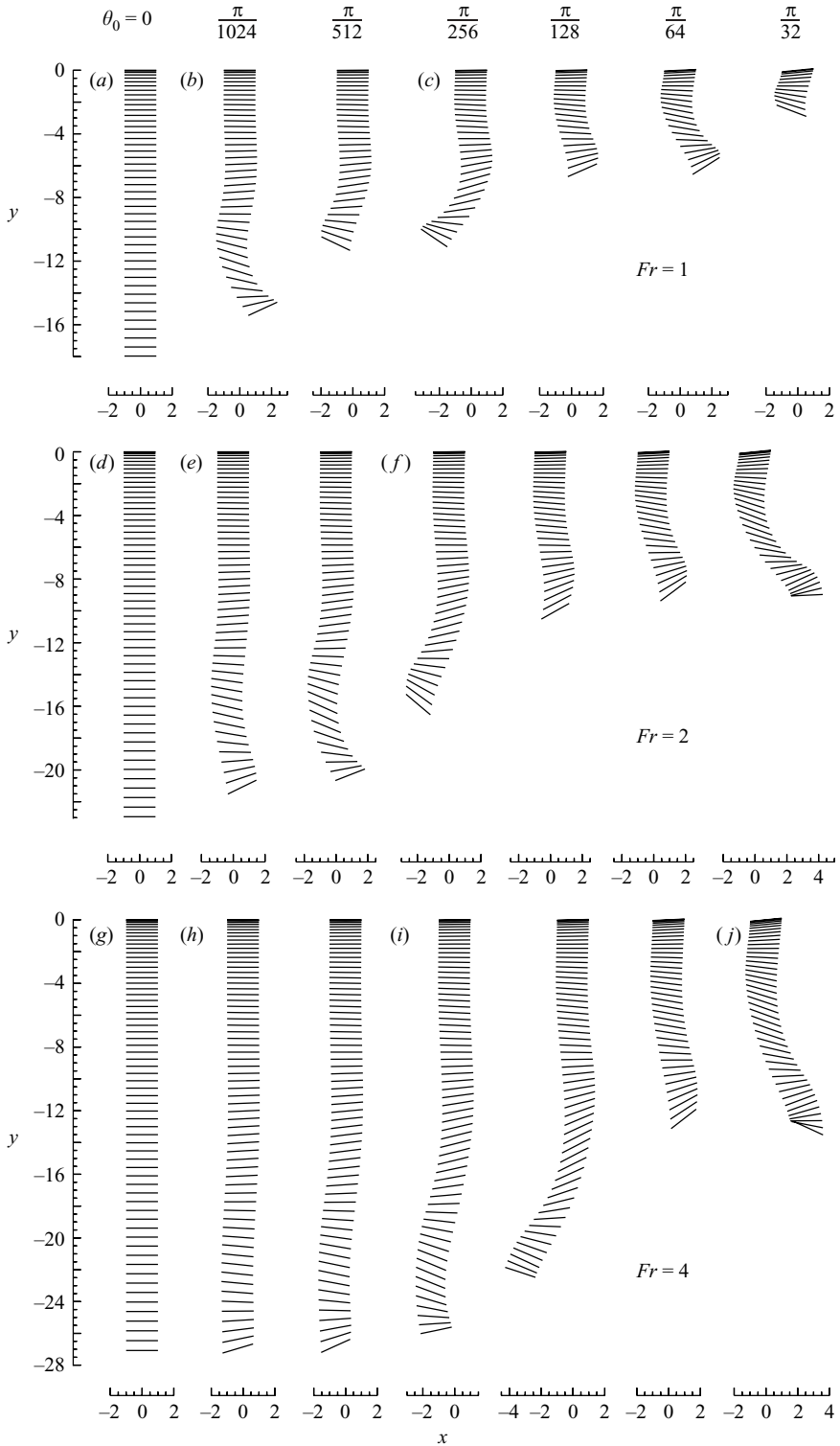
FIGURE 6. The trajectories of a falling flat plate after its release from rest. The trajectories are shown for $\theta_0 = 0$, $\pi/1024$, $\pi/512$, $\pi/256$, $\pi/128$, $\pi/64$, and $\pi/32$ for each of the three modified Froude numbers $Fr = 1$, 2, and 4. The labelled trajectories are discussed further in the text.
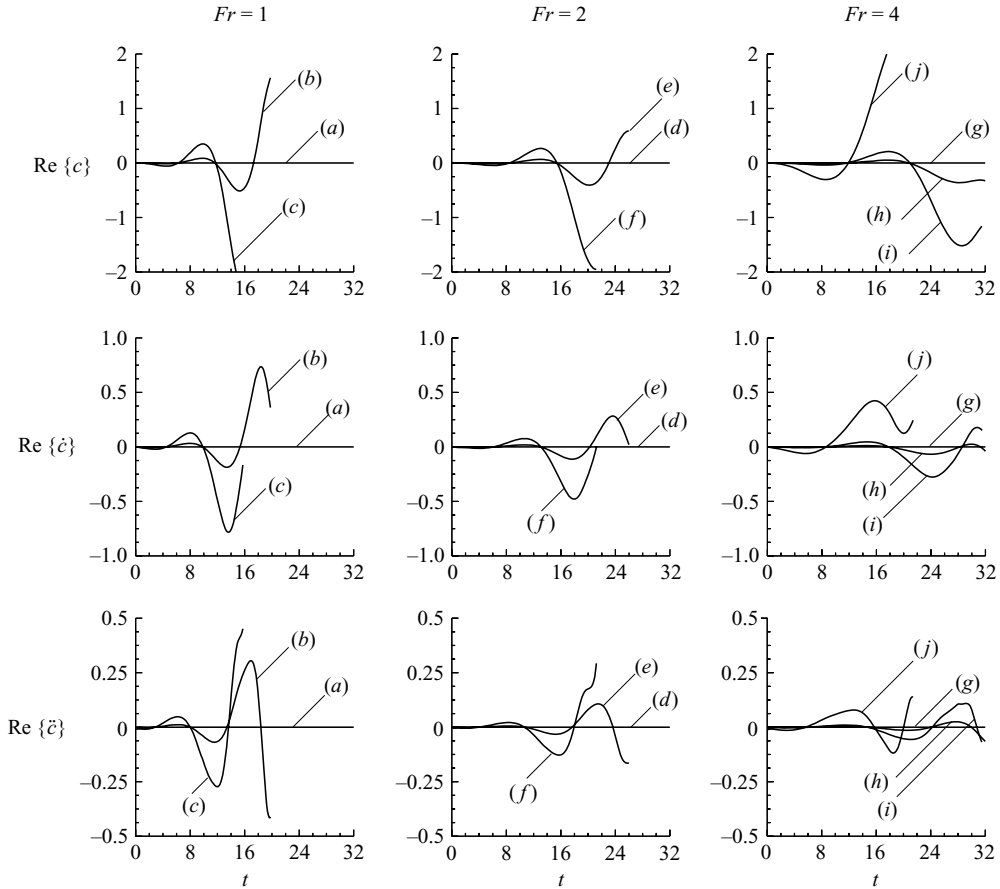
FIGURE 7. The motion of a falling plate after release from rest; examples (a)–(j). The functions $\mathrm{Re}\{c(t)\}$, $\mathrm{Re}\{\dot{c}(t)\}$, and $\mathrm{Re}\{\ddot{c}(t)\}$ are plotted for modified Froude numbers (a)–(c) $Fr = 1$, (d)–(f) $Fr = 2$, and (g)–(j) $Fr = 4$ and initial angles $(a)(d)(g)$ $\theta_0 = 0$, $(b)(e)(h)$ $\theta_0 = \pi/1024$, $(c)(f)(i)$ $\theta_0 = \pi/256$, and (j) $\theta_0 = \pi/32$.

wake is visualized by showing the position of the plate and the two free vortex sheets at a number of different times. Figure 13 shows the corresponding edge circulations $\Gamma_\pm(t)$, the total shed circulation $\left[\Gamma_\pm(t)\right]_-^+$, and the shedding rates $\dot{\Gamma}_\pm(t)$. Figure 14 shows the aerodynamic normal force $\mathbb{F}(t)$ and torque $\mathbb{T}(t)$. Figures 15 and 16 feature example (j) only ($Fr = 4$ and $\theta_0 = \pi/32$). Figure 15 shows the late-time evolution of the vortex wake and figure 16 shows the corresponding aerodynamic normal force $\mathbb{F}(t)$ and aerodynamic torque $\mathbb{T}(t)$. Finally, in figures 17 and 18, example (j) is compared to the corresponding solutions obtained from two more primitive models: (k) a quasi-steady model, and (l) a point-vortex model. The effects of increasing and decreasing the regularization parameter to (m) $\delta = 0.3$ and (n) $\delta = 0.1$ are also considered.

5.1. *Symmetric calculations*

We begin by describing the symmetric examples (a), (d), and (g), in which $\theta_0 = 0$. In these cases the plate remains perfectly horizontal throughout the computation ($\theta_0 = \dot{\theta}_0 = \ddot{\theta}_0 = 0$) and falls vertically downward ($\mathrm{Re}\{c\} = \mathrm{Re}\{\dot{c}\} = \mathrm{Re}\{\ddot{c}\} = 0$) with increasing speed. See figures 6, 7, 8, and 9. For times $t < 1$, the downward
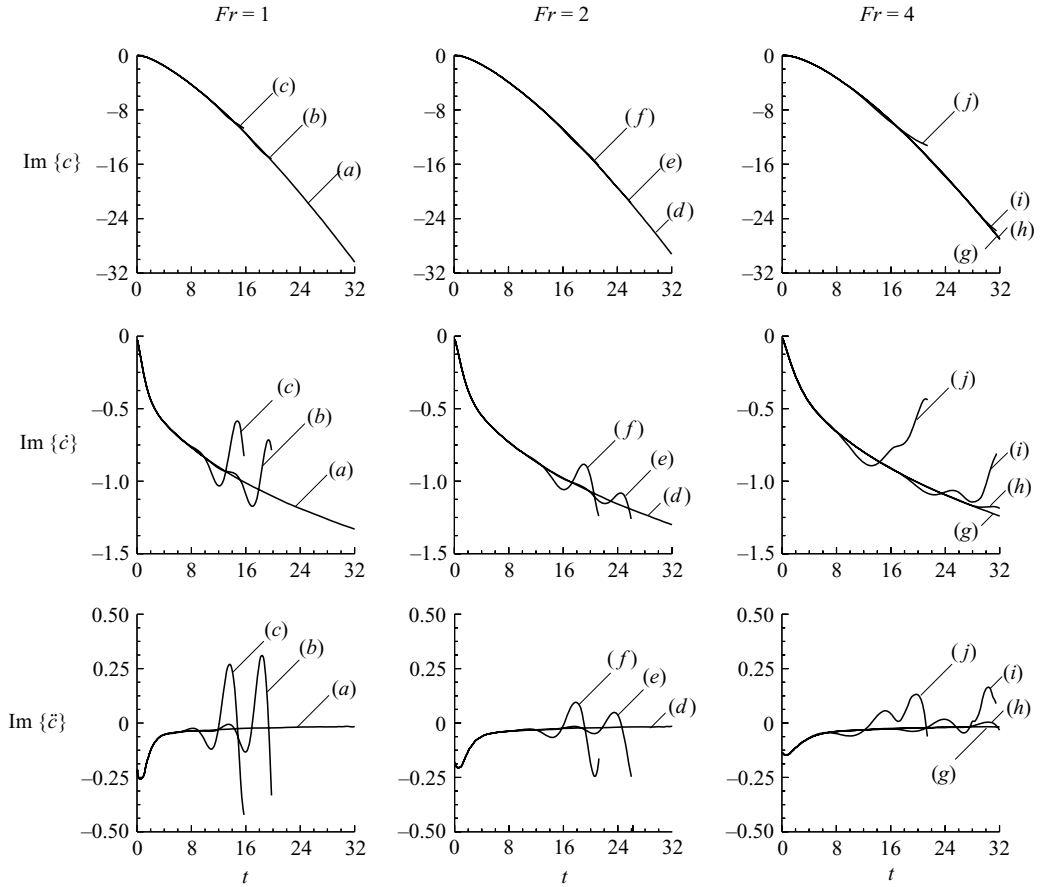
FIGURE 8. The motion of a falling plate after release from rest; examples (a)–(j). The functions $\text{Im}\{c(t)\}$, $\text{Im}\{\dot{c}(t)\}$, and $\text{Im}\{\ddot{c}(t)\}$ are plotted for modified Froude numbers (a)–(c) $Fr = 1$, (d)–(f) $Fr = 2$, and (g)–(j) $Fr = 4$ and initial angles $(a)(d)(g)$ $\theta_0 = 0$, $(b)(e)(h)$ $\theta_0 = \pi/1024$, $(c)(f)(i)$ $\theta_0 = \pi/256$, and (j) $\theta_0 = \pi/32$.

acceleration of the plate remains approximately constant and the wake consists of the two small starting vortices that are shed at $t = 0$. See figures 10(a), 11(d), 12(g). An adjustment period then follows during which the downward acceleration of the plate rapidly decreases whilst the two starting vortices grow and begin to interact with each other. In example (a) this adjustment period lasts until around $t = 4$ whereas in example (g) is lasts until around $t = 8$. From this point onward, the gravitational and aerodynamic forces on the plate remain in rough balance and the starting vortices continue to grow and lengthen while the shedding rate slowly decreases. See figure 13. Having said this, the gravitational force on the plate is not quite matched by the aerodynamic drag on the plate and so its downward velocity continues to grow albeit at a slowing rate. As a result, it is difficult to identify a well-defined terminal velocity for the plate. However, by the end of each computation the downward velocity has reached around one and a quarter times the value estimated in §1 and the plate has fallen through between 12 and 15 times its own chord length.

At this point it is informative to note that a given instant in non-dimensional time t does not correspond with the same instant in dimensional time at differing
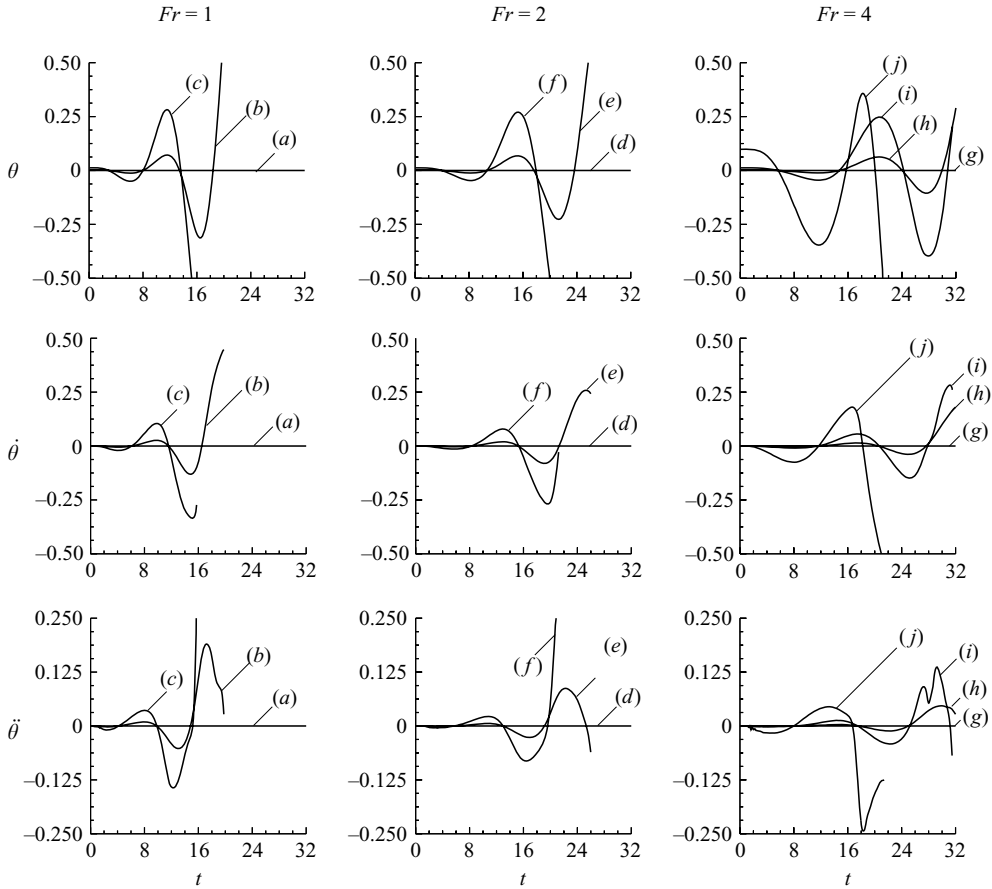
FIGURE 9. The motion of a falling plate after release from rest; examples (a)–(j). The functions $\theta(t)$, $\dot{\theta}(t)$, and $\ddot{\theta}(t)$ are plotted for modified Froude numbers (a)–(c) $Fr = 1$, (d)–(f) $Fr = 2$, and (g)–(j) $Fr = 4$ and initial angles $(a)(d)(g)$ $\theta_0 = 0$, $(b)(e)(h)$ $\theta_0 = \pi/1024$, $(c)(f)(i)$ $\theta_0 = \pi/256$, and (j) $\theta_0 = \pi/32$.

modified Froude numbers. This is because time was originally non-dimensionalized with respect to the time scale

$$\frac{L}{U} = \sqrt{\frac{L\rho_s}{g(\rho_s - \rho_f)Fr}}, \qquad (5.1)$$

which itself depends on the modified Froude number, among other things. With this in mind, we note that example (a) represents twice as long a period of dimensional time as example (g), all other things being equal. As a result, figure 8 does not contradict our everyday experience that heavier objects fall faster through fluids than lighter objects. Instead, it confirms that an initially horizontal plate with $Fr = 4$ will fall almost as far as one with $Fr = 1$ in half the time.

5.2. *Asymmetric calculations*

We next introduce a small degree of asymmetry by setting $\theta_0 = \pi/1024$ and considering examples (b), (e), and (h). Again, the plate begins by falling almost vertically downward and two small starting vortices are shed as before. See figures 10(b), 11(e), and 12(h).
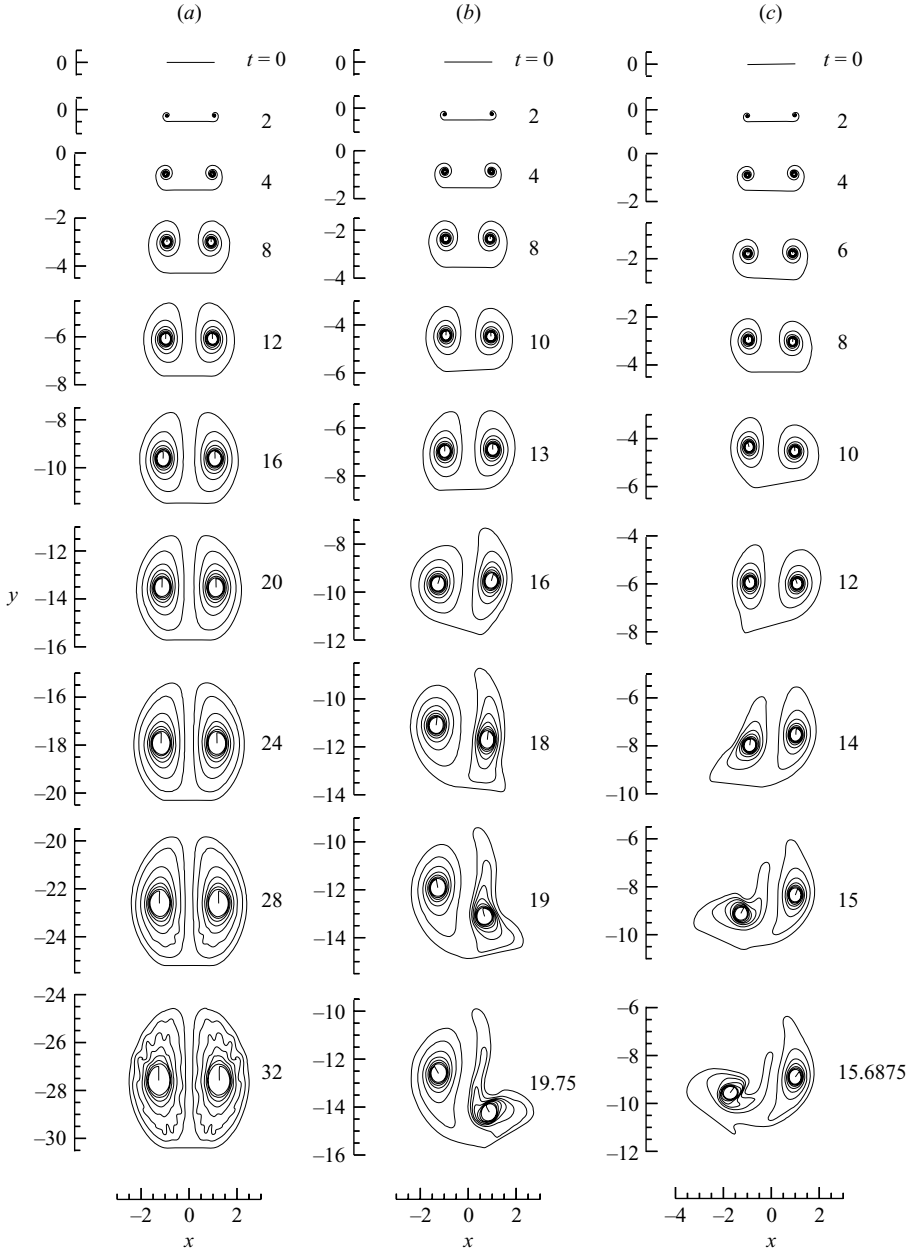
FIGURE 10. Examples (*a*), (*b*), and (*c*). The trailing vortex sheets left behind a falling flat plate with $Fr = 1$. The wake is visualized at times $t = 0, 2, 4, 8, 12, 16, 20, 24, 28,$ and 32 for (*a*) $\theta_0 = 0$. At times $t = 0, 2, 4, 8, 10, 13, 16, 18, 19,$ and 19.75 for (*b*) $\theta_0 = \pi/1024$. And at times $t = 0, 2, 4, 6, 8, 10, 12, 14, 15,$ and 15.6875 for (*c*) $\theta_0 = \pi/256$.

However, this slightly asymmetric configuration soon becomes unstable to growing oscillations. See figures 6–9. The oscillations are amplified by the following mechanism.

Due to the slight asymmetry in the initial conditions, a small component of the aerodynamic normal force $\mathbb{F}(t)$ is immediately available to accelerate the plate sideways. See figure 14. This, together with the fact that the plate much prefers to
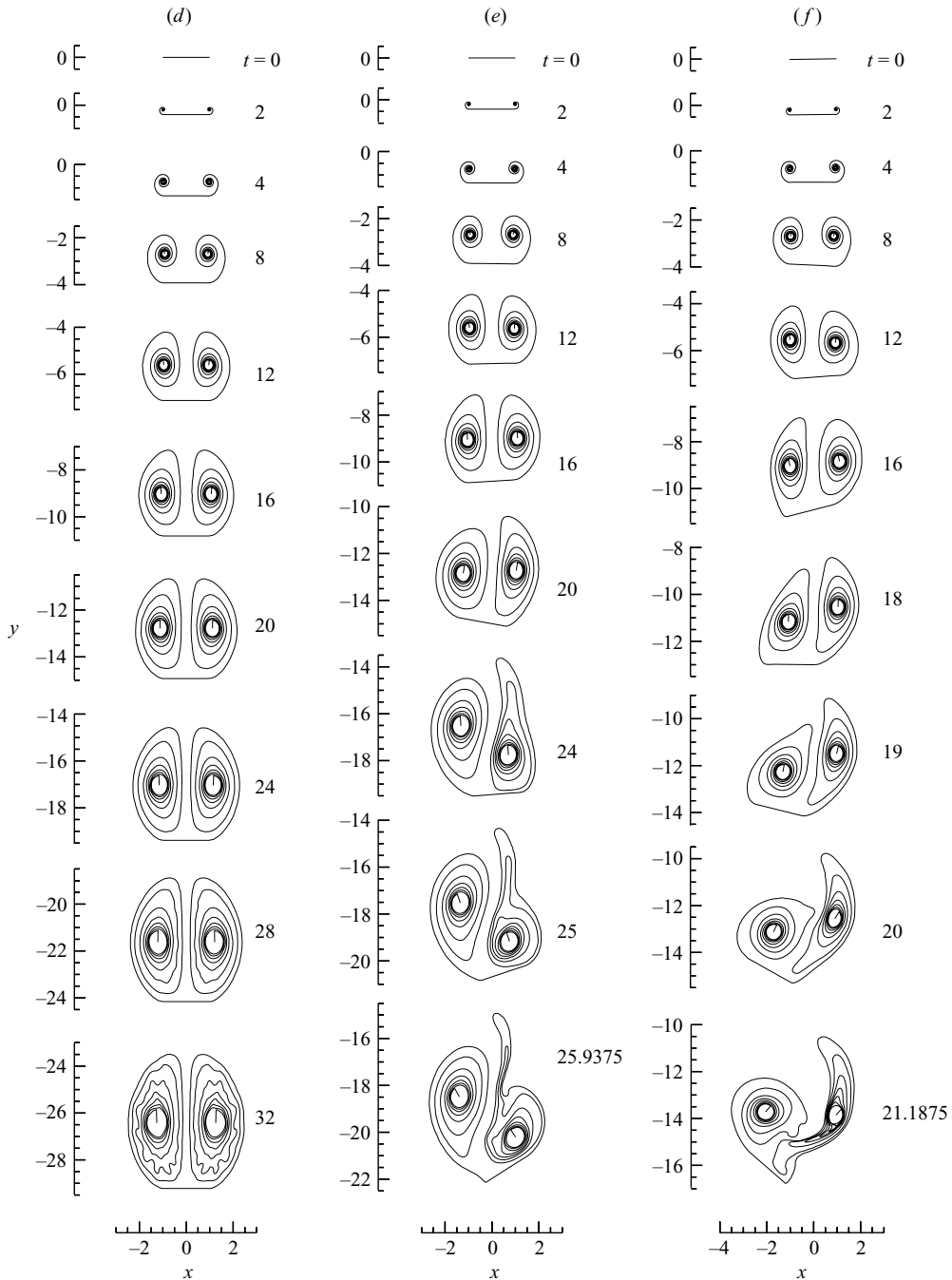
FIGURE 11. Examples (*d*), (*e*), and (*f*). The trailing vortex sheets left behind a falling flat plate with $Fr = 2$. The wake is visualized at times $t = 0, 2, 4, 8, 12, 16, 20, 24, 28,$ and 32 for (*d*) $\theta_0 = 0$. At times $t = 0, 2, 4, 8, 12, 16, 20, 24, 25,$ and 25.9375 for (*e*) $\theta_0 = \pi/1024$. And at times $t = 0, 2, 4, 8, 12, 16, 18, 19, 20,$ and 21.1875 for (*f*) $\theta_0 = \pi/256$.

slip sideways through the fluid as opposed to broadside on, causes one of the two starting vortices to be left slightly behind. In turn, a correcting aerodynamic torque is set up, due to the resulting asymmetry in the wake, and the plate is brought
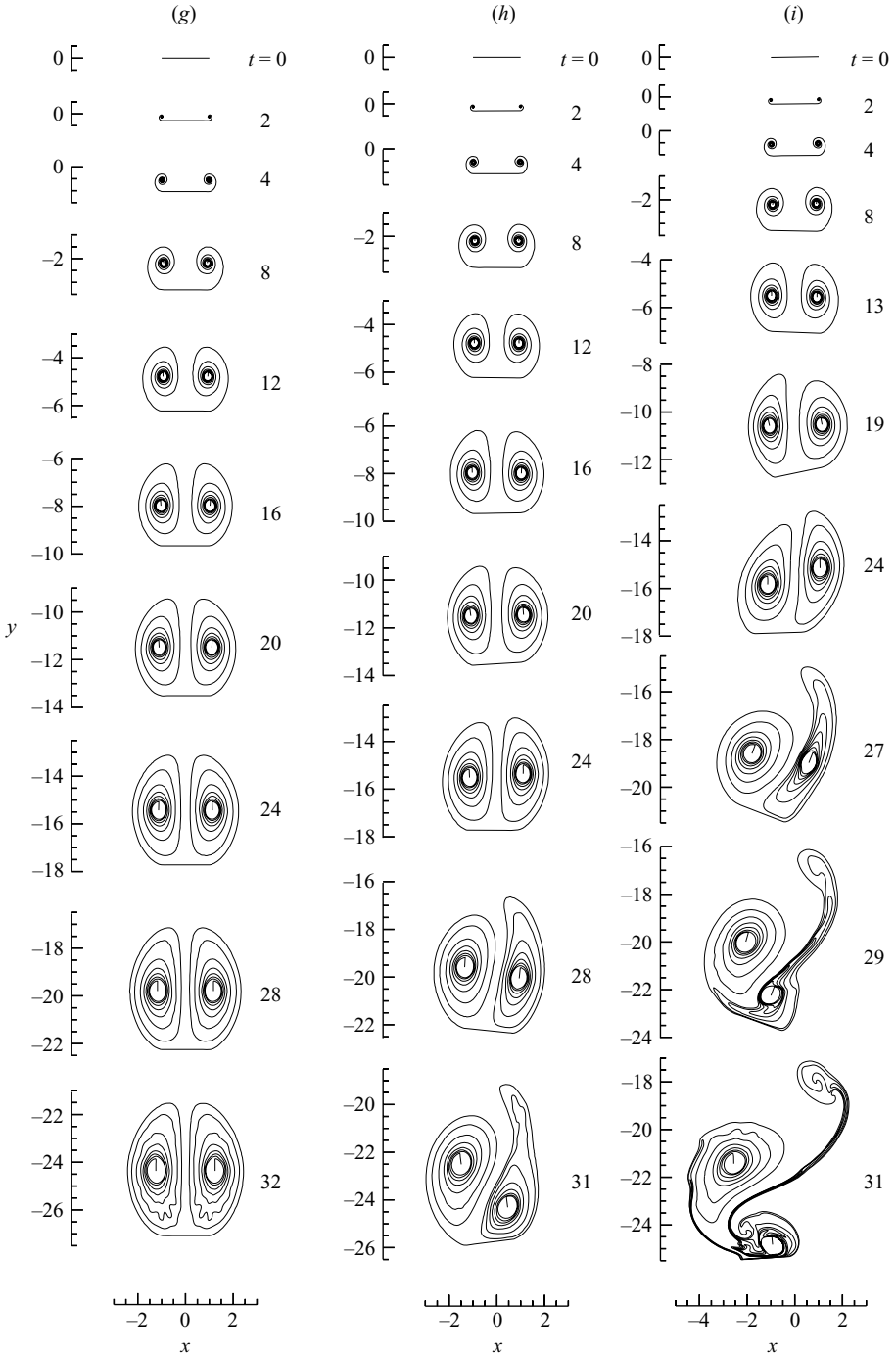
FIGURE 12. Examples (*g*), (*h*), and (*i*). The trailing vortex sheets left behind a falling flat plate with $Fr = 4$. The wake is visualized at times $t = 0, 2, 4, 8, 12, 16, 20, 24, 28$, and 32 for (*g*) $\theta_0 = 0$. At times $t = 0, 2, 4, 8, 12, 16, 20, 24, 28$, and 31 for (*h*) $\theta_0 = \pi/1024$. And at times $t = 0, 2, 4, 8, 13, 19, 24, 27, 29$, and 31 for (*i*) $\theta_0 = \pi/256$.
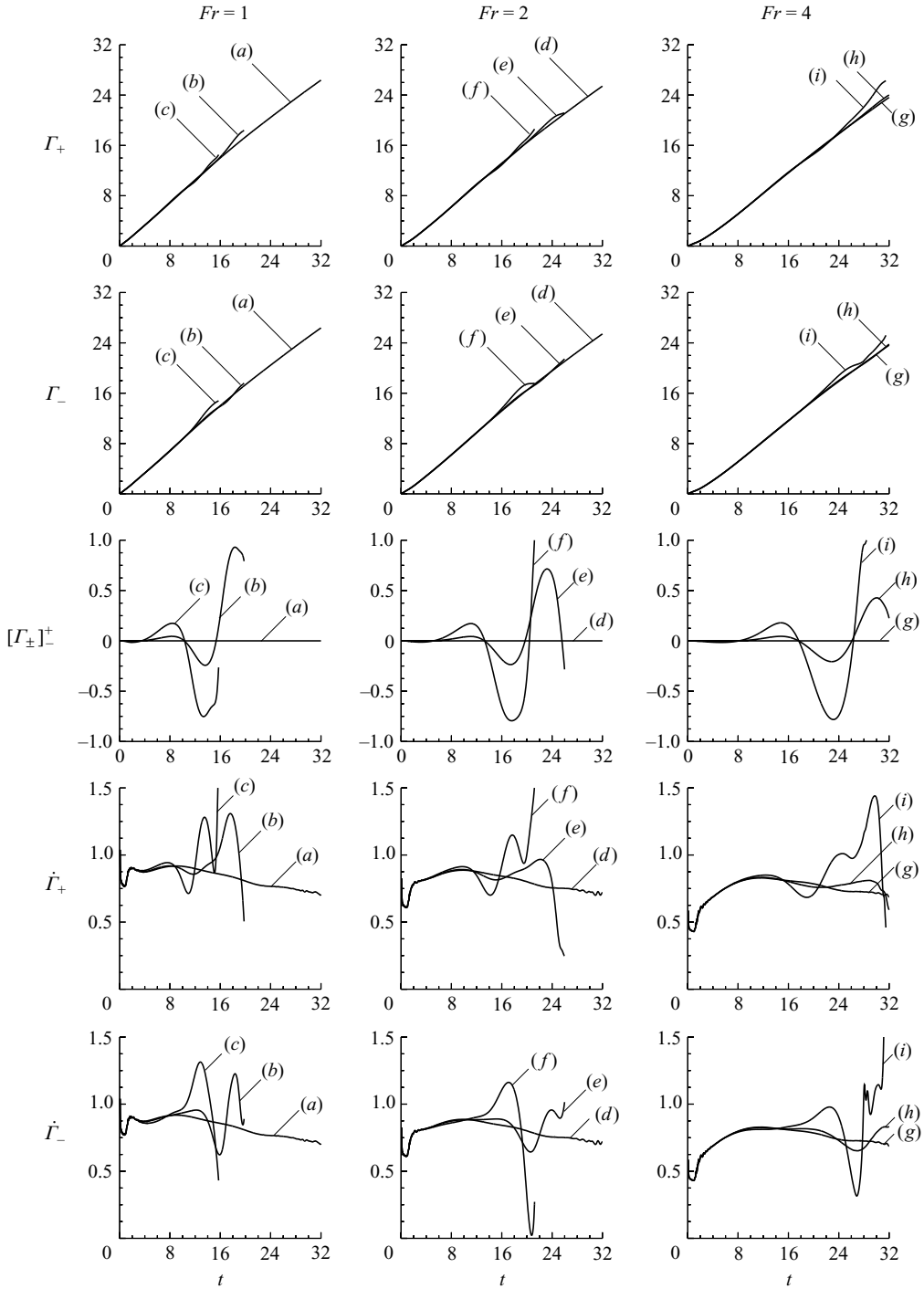
FIGURE 13. The circulation around a falling plate after release from rest; examples (a)–(i). The functions $\Gamma_+(t)$ and $\Gamma_-(t)$, the bound circulation $[\Gamma_\pm(t)]_-^+$, and the shedding rates $\dot{\Gamma}_+(t)$, and $\dot{\Gamma}_-(t)$ are plotted for modified Froude numbers (a)–(c) $Fr = 1$, (d)–(f) $Fr = 2$, and (g)–(i) $Fr = 4$ and initial angles $(a)(d)(g)$ $\theta_0 = 0$, $(b)(e)(h)$ $\theta_0 = \pi/1024$, and $(c)(f)(i)$ $\theta_0 = \pi/256$.
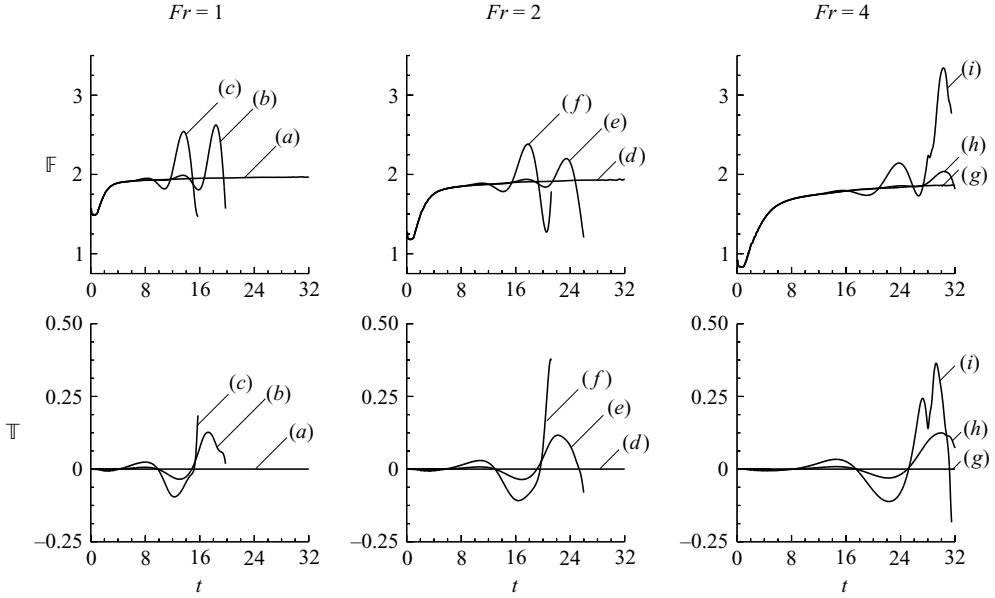
FIGURE 14. The aerodynamic normal force and torque on a falling plate after release from rest; examples (a)–(i). The functions $\mathbb{F}(t)$ and $\mathbb{T}(t)$ are plotted for modified Froude numbers (a)–(c) $Fr = 1$, (d)–(f) $Fr = 2$, and (g)–(i) $Fr = 4$ and initial angles $(a)(d)(g)$ $\theta_0 = 0$, $(b)(e)(h)$ $\theta_0 = \pi/1024$, and $(c)(f)(i)$ $\theta_0 = \pi/256$.

back toward a horizontal position. The plate's inertia then causes it to overshoot the horizontal and the component of the aerodynamic drag that was originally available to accelerate the plate sideways is then available to decelerate it. This increases the impact of the asymmetry in the wake and enhances the angular overshoot, making more pronounced deceleration possible. The process is then repeated in the opposite direction at larger amplitude and so on. On top of the primary (angular and side-to-side) oscillations described above sit secondary oscillations, of twice the frequency, in the downward velocity of the plate. See figure 8. These are driven by oscillations in the aerodynamic normal force on the plate $\mathbb{F}(t)$, which are in turn driven by the primary angular oscillations, the aerodynamic drag on the plate being instantaneously maximal when $\theta(t) = 0$, that is twice per primary period. See figures 9 and 14.

In general, the amplitude of all of the above oscillations grows exponentially until one of two things happens: either the effective angle of attack becomes too small or a large-scale reconfiguration of the wake is triggered. Unfortunately, each of these events is usually accompanied by the imminent violation of equation (4.33), in which case the computation is stopped.

In examples (c), (f), and (i) the degree of asymmetry is increased further by setting $\theta_0 = \pi/256$. Again, the initial motion of the plate becomes immediately unstable to growing oscillations and the solutions are qualitatively similar to those already presented, the only notable difference being the larger amplitude of oscillation.

If we consider all of the solutions presented thus far we can identify two clear trends. First, the frequency of the growing oscillations remains independent of amplitude at fixed Fr, at least for the relatively small amplitudes considered here. And second, the frequency of oscillation scales in direct proportion with the inverse square root of the modified Froude number $1/\sqrt{Fr}$. This scaling is to be expected from equations (2.3)
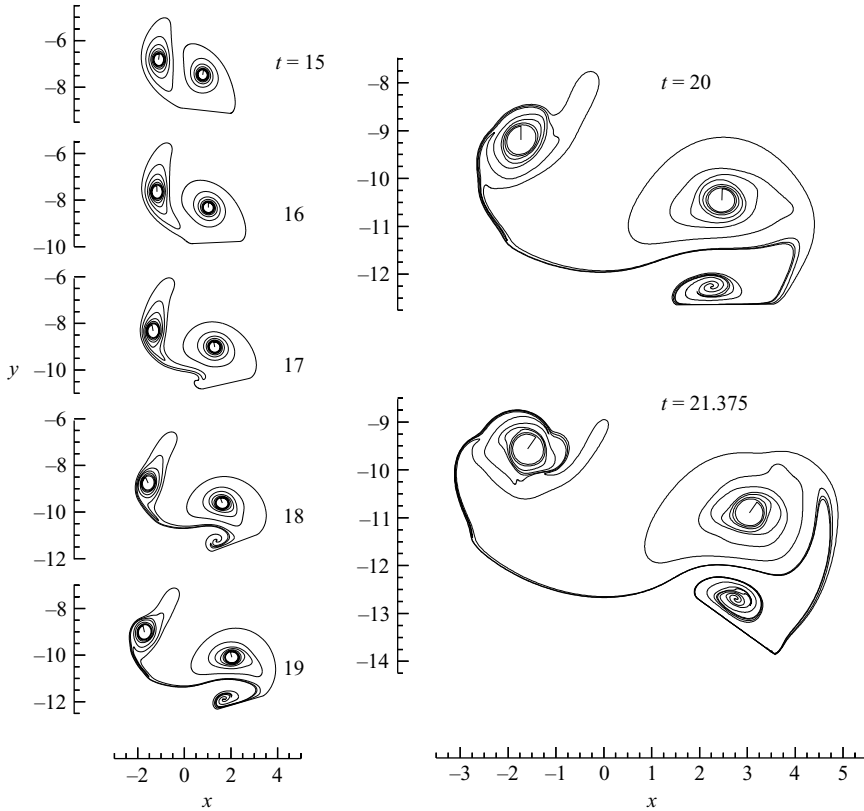
FIGURE 15. Example (*j*). The trailing vortex sheets left behind a falling flat plate with $Fr = 4$ and $\theta_0 = \pi/32$. The wake is visualized at times $t = 15, 16, 17, 18, 19, 20$, and 21.375; the frames for $t = 20$ and 21.375 are shown magnified by a factor of 2.

and (2.4) and, in view of equation (5.1), suggests that the dimensional frequency of the oscillations is independent of the modified Froude number, at least for the larger modified Froude numbers considered here. Of course, this is only true if all other quantities in equation (5.1) are held fixed. These trends are in agreement with those previously identified experimentally by Mahadevan *et al.* (1999).

Finally, we move on to consider example (*j*), in which a large-scale reconfiguration of the wake is triggered without violating equation (4.33). At early times, the solution evolves in a familiar way, exhibiting growing oscillations, until a new kind of event occurs between $t = 16$ and $t = 18$. As the plate swings from left to right, the presence of the large leading-edge vortex, shed during the first half of the oscillation, induces a marked increase in the rate of shedding at the trailing-edge. The newly shed circulation then quickly rolls up into a new trailing-edge vortex and the existing trailing-edge vortex is effectively shed between $t = 18$ and $t = 19$. See figures 6(*j*) and 15. The low-pressure core in the newly shed vortex then exerts a large negative aerodynamic torque on the plate, see figure 16, and the plate begins to rotate in a clockwise direction, eventually overshooting the horizontal at around $t = 20$. This orientation change completely disrupts the familiar side-to-side oscillation of the plate and presumably initiates another glide from left to right. Unfortunately, the calculation is stopped at $t = 21.375$ due to a violation of equation (4.33) at the leading edge. Despite its limited duration, the calculation in example (*j*) is encouraging since it
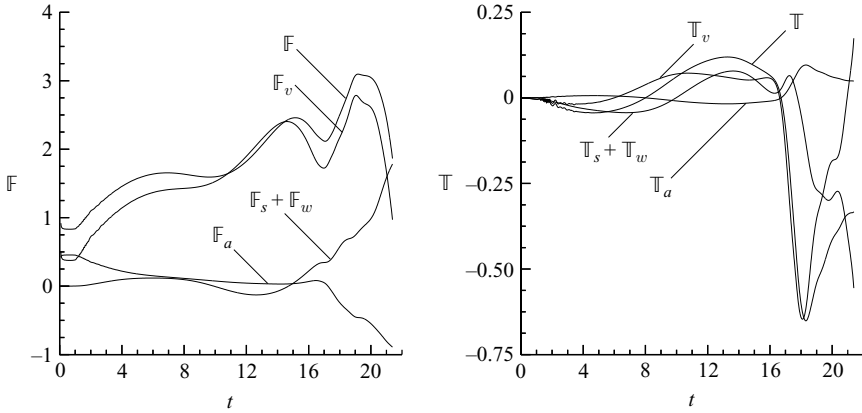
FIGURE 16. Example (*j*). The total aerodynamic normal force $\mathbb{F}(t)$ and torque $\mathbb{T}(t)$ on a falling flat plate after release from rest with $Fr = 4$ and $\theta_0 = \pi/32$. Also plotted, are the corresponding acceleration reactions $\mathbb{F}_a(t)$ and $\mathbb{T}_a(t)$, unsteady vortical contributions $\mathbb{F}_v(t)$ and $\mathbb{T}_v(t)$, and quasi-steady contributions $\mathbb{F}_s(t) + \mathbb{F}_w(t)$ and $\mathbb{T}_s(t) + \mathbb{T}_w(t)$.
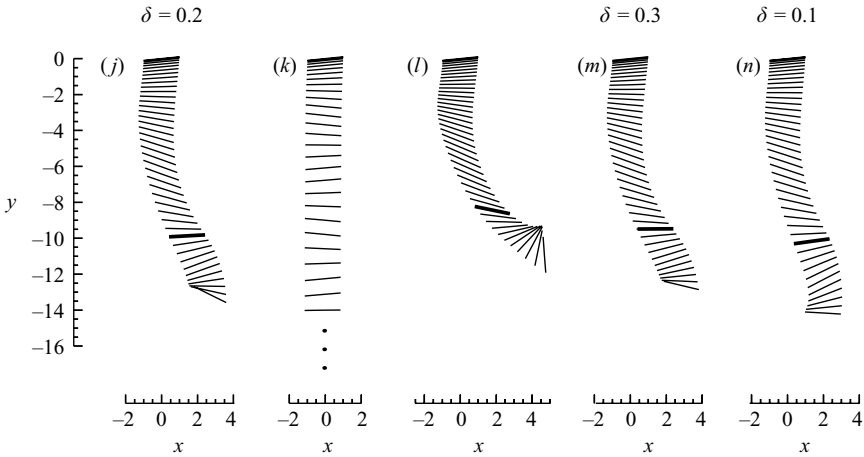

FIGURE 17. Examples (*j*)–(*n*). The trajectories of a falling flat plate after its release from rest with $Fr = 4$ and $\theta_0 = \pi/32$. The wake is modelled as (*j*) two regularized vortex sheets with $\delta = 0.2$, (*k*) no wake, (*l*) a pair of point vortices, (*m*) two regularized vortex sheets with $\delta = 0.3$, and (*n*) two regularized vortex sheets with $\delta = 0.1$. The plate positions at $t = 16$ are highlighted.

shows that the spontaneous occurrence of a fluid dynamical event (in this case the shedding of a new trailing-edge vortex) can strongly influence the subsequent motion of the plate, thereby illustrating the essentially interactive nature of the problem under consideration.

5.3. *The role of added mass*

We next examine the relative importance of the effects of added mass in the falling card problem since for some time now it has been unclear how important such effects are in comparison with those associated with vortex shedding. Indeed, added mass effects have been included in previous studies of the falling card problem (in the absence of vortex shedding) most notably by Mahadevan (1996).
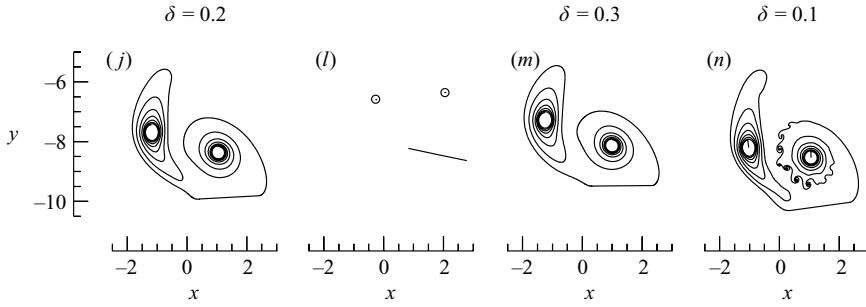
FIGURE 18. Examples (*j*), (*l*), (*m*), and (*n*). The wake behind a falling flat plate at $t = 16$ after its release from rest with $Fr = 4$ and $\theta_0 = \pi/32$. The wake is modelled as (*j*) two regularized vortex sheets with $\delta = 0.2$, (*l*) a pair of point vortices, (*m*) two regularized vortex sheets with $\delta = 0.3$, and (*n*) two regularized vortex sheets with $\delta = 0.1$.

We begin by noting that the direct use of equation (A 9) in equations (A 5) and (A 6), followed by the use of the integral constraints (2.16) and (2.17), leads to exact expressions for the unsteady normal force and torque $\mathbb{F}_u(t)$ and $\mathbb{T}_u(t)$ in the form

$$\mathbb{F}_u(t) \equiv \mathbb{F}_a(t) + \mathbb{F}_v(t) = -\pi \dot{v}(t) + \left[\int_0^{\Gamma_\pm(t)} \mathrm{Re}\left\{ \partial_t z_\pm(\Lambda, t)\delta_1(z_\pm(\Lambda, t)) \right\} \mathrm{d}\Lambda \right]_-^+, \quad (5.2)$$

$$\mathbb{T}_u(t) \equiv \mathbb{T}_a(t) + \mathbb{T}_v(t) = -\frac{\pi}{8} \ddot{\theta}(t) + \left[\int_0^{\Gamma_\pm(t)} \mathrm{Re}\left\{ \partial_t z_\pm(\Lambda, t)\delta_2(z_\pm(\lambda, t)) \right\} \mathrm{d}\Lambda \right]_-^+, \quad (5.3)$$

where $\delta_1(z)$ and $\delta_2(z)$ are as defined in equation (A 10). The first terms on the right-hand sides of equations (5.2) and (5.3) are the so-called *acceleration reactions* and are henceforth denoted $\mathbb{F}_a(t)$ and $\mathbb{T}_a(t)$. They are proportional to the normal and angular accelerations of the plate and are therefore responsible for the effect known as added mass. The remaining terms, denoted $\mathbb{F}_v(t)$ and $\mathbb{T}_v(t)$, are novel and arise as a direct result of the relative motion between the plate and its vortex wake. Our main aim here is to find out which, if any, of the terms in equations (5.2) and (5.3) are dominant within the context of the falling card problem.

Again we consider example (*j*). For small times $t < 1$, we find that the total aerodynamic force $\mathbb{F}(t)$ is dominated by the acceleration reaction $\mathbb{F}_a(t)$, in line with the predictions of §3. However, as the plate's downward velocity increases $\mathbb{F}_a(t)$ slowly decreases whilst the unsteady vortical force $\mathbb{F}_v(t)$ quickly increases and soon becomes strongly dominant. See figure 16. This dominance is maintained throughout the calculation even after the subsequent reconfiguration in the wake, which is triggered at around $t = 16$. In contrast, the summed total of the forces $\mathbb{F}_s(t)$ and $\mathbb{F}_w(t)$ remains effectively negligible until $t = 16$, after which it grows steadily. However, this growth is largely negated by a simultaneous drop in the acceleration reaction force $\mathbb{F}_a(t)$. The total aerodynamic torque $\mathbb{T}(t)$ is similarly dominated by the unsteady vortical torque $\mathbb{T}_v(t)$, although the torques $\mathbb{T}_s(t)$ and $\mathbb{T}_w(t)$ also play a significant role.

It is therefore clear, at least within the context of the example considered, that the unsteady vortical loads $\mathbb{F}_v(t)$ and $\mathbb{T}_v(t)$ dominate the evolution of the plate's trajectory, whereas, the other loads, including the acceleration reactions, play important roles only intermittently.

5.4. *A comparison with two more primitive models*

Having noted that the unsteady vortical loads $\mathbb{F}_v(t)$ and $\mathbb{T}_v(t)$ are dominant in example (*j*), it proves interesting to compare that solution with those obtained through the use of more primitive models. A number of such models can be derived directly from the governing equations (2.1)–(2.20). To illustrate the point we first rewrite the equations of motion for the falling plate in the rest frame of the plate. In this frame, equations (2.3) and (2.4) can be written as the first-order system

$$\dot{c}(t) = (\tau(t) + i\nu(t))\, e^{i\theta(t)}, \tag{5.4}$$

$$\dot{\theta}(t) = \omega(t), \tag{5.5}$$

$$Fr\,\dot{\tau}(t) = Fr\,\nu(t)\omega(t) - \sin\theta(t), \tag{5.6}$$

$$\left(\tfrac{1}{2}\pi + Fr\right)\dot{\nu}(t) = \tfrac{1}{2}\left(\mathbb{F}_v + \mathbb{F}_w\right) - \tfrac{1}{2}\tau(t)[\Gamma_\pm(t)]_-^+ - Fr\,\tau(t)\omega(t) - \cos\theta(t), \tag{5.7}$$

$$\left(\tfrac{1}{16}\pi + \tfrac{1}{3}Fr\right)\dot{\omega}(t) = \tfrac{1}{2}\left(\mathbb{T}_v + \mathbb{T}_w\right) - \tfrac{\pi}{2}\tau(t)\nu(t), \tag{5.8}$$

where $\omega(t)$ denotes the angular velocity of the plate. As an aside, we note that equations (5.4)–(5.8) are effectively the same as those previously derived by Mahadevan (1996). However, in contrast with that study both the unsteady and steady effects of plate's vortical wake are now included. To aid comparison with the study of Mahadevan (1996), we also mention that no added mass effect appears in equation (5.6) because, as far as the surrounding fluid is concerned, the flat plate considered here has no thickness.

Starting from equations (5.4)–(5.8), together with equations (2.1), (2.9)–(2.19), (5.2)–(5.3), and (A 7)–(A 10), it is straightforward to derive a number of more primitive models, either by entirely neglecting or approximately representing the complicated wake-induced terms. For example, a quasi-steady model that neglects the plate's vortical wake altogether can be derived by simply dropping the terms $\mathbb{F}_v(t)$, $\mathbb{F}_w(t)$, $\mathbb{T}_v(t)$, and $\mathbb{T}_w(t)$ from the right-hand side of equations (5.7) and (5.8) and by choosing the negative of the bound circulation $[\Gamma_\pm(t)]_-^+$ to be

$$[\Gamma_\pm(t)]_-^+ = \begin{cases} \pi\omega(t) + 2\pi\nu(t), & \tau(t) < 0 \\ \pi\omega(t) - 2\pi\nu(t), & \tau(t) > 0. \end{cases} \tag{5.9}$$

This particular choice instantaneously imposes the steady Kutta condition at the trailing edge. Another simple model, which approximately represents the plate's vortical wake using two point vortices (one associated with each edge), can be derived by performing the formal replacement

$$z_\pm(\Gamma, t) \longrightarrow z_\pm(t), \tag{5.10}$$

in equations (2.9)–(2.19), (5.2)–(5.3), and (A 9). Then $z_+(t)$ and $z_-(t)$ denote the positions of the two point vortices, and any circulation that is shed from either of the plate's two sharp edges is effectively transported into the core of the corresponding point vortex instantaneously.

We next compare the solutions obtained by using the two primitive models described above with example (*j*). For completeness, we also consider the effects of altering the regularization parameter δ. Figure 17 shows the trajectory of the falling plate for $Fr = 4$ and $\theta_0 = \pi/32$ as obtained using the different models. Each plot is a collage of frames showing the plate's position at the times $t = 0, 0.5, 1, 1.5, 2$, etc. The trajectories are labelled (*j*)–(*n*) and correspond to (*j*) the regularized vortex-sheet

model with $\delta = 0.2$ (repeated from figure 6(j)), (k) the quasi-steady model with no wake, (l) the point-vortex model, (m) the regularized vortex-sheet model with $\delta = 0.3$, and (n) the regularized vortex-sheet model with $\delta = 0.1$. Figure 18 shows the corresponding plate positions and wake configurations at $t = 16$.

In example (k), the plate quickly accelerates under gravity and, due to the lack of any effective aerodynamic drag, continues to accelerate ballistically, although slight angular and side-to-side oscillations are also present. The calculation clearly shows that the omission of the vortical forces in equations (5.7) and (5.8) is ill-advised. In contrast, the point-vortex model of example (l) does rather better. For $t < 10$ it captures the downward, angular, and side-to-side motions well. See figure 17(l). However, at later times the predicted position of the rightmost vortex becomes inaccurate (see figure 18(l)) and, more importantly, the inability of the model to predict the spontaneous shedding event that occurs at $t = 16$ allows the initiation of an erroneous tumbling event. Examples (m) and (n) are included only to illustrate the point that altering the regularization parameter δ has little effect on the macroscopic properties of the plate's trajectory, although, the details of the distribution of vorticity in the wake are notably altered for $\delta = 0.1$ due to the effective re-introduction of the Kelvin–Helmholtz instability at smaller scales. See figure 18(m). For a more detailed account of the effects of altering the regularization parameter δ, the interested reader is referred to the work of Krasny (1986a).

It is therefore clear that the simple primitive models considered here are largely unsatisfactory, at least in the context of the falling card problem. However, a refined version of the point-vortex model, modified to allow for the occurrence of spontaneous shedding events, may yet prove useful.

6. Conclusions

In summary, we have successfully modelled the separated flow of an inviscid fluid around a falling flat plate using a boundary integral formulation for the complex-conjugate velocity field $\Phi(z, t)$. The resulting steady and unsteady aerodynamic forces were analytically incorporated into the equations of motion for the plate. The equations of motion for the surrounding fluid and vortical wake were also derived and the flow solution was constructed so as to automatically satisfy the kinematic boundary condition, the unsteady Kutta condition, Kelvin's circulation theorem, and the proper far-field boundary conditions. The resulting system of governing equations was shown to be essentially implicit in the unknown accelerations $\ddot{c}(t)$ and $\ddot{\theta}(t)$, which reflects the interactive nature of the problem in hand. However, the linearity of the relevant equations in those unknowns eventually allowed the coupled system of governing equations to be rewritten in an essentially explicit form. Finally, the unsteady aerodynamic loads were shown to depend not only on the usual acceleration reactions, which lead to the effect known as added mass, but also on novel unsteady vortical loads, which arise due to relative motion between the plate and its wake.

For small times $t < 1$, an asymptotic solution to the full system of governing equations was derived and the plate's motion was shown to depend only on gravity and the acceleration reaction of the fluid; terms due to the unsteady shedding of vorticity from the plate's two sharp edges were shown to be of higher order.

For larger times, a novel numerical treatment of the full system of evolution equations was proposed and implemented and the results of several example calculations were presented. Unfortunately, the scope of the proposed numerical method turned out to be somewhat limited, due to the spontaneous occurrence of a

specific type of backflow event. However, long-time solutions for $Fr > 1$ and $\theta_0 < \pi/32$ were successfully obtained. In the parameter ranges considered, all asymmetric solutions were found to be unstable to growing oscillations, the non-dimensional frequency of which scaled with $1/\sqrt{Fr}$.

Appendix. Alternative expressions for $\mathbb{F}(t)$ and $\mathbb{T}(t)$

As reported in Jones (2003), one can derive alternative expressions for the normal force $\mathbb{F}(t)$ and the torque $\mathbb{T}(t)$ that effectively replace equations (2.5) and (2.6); they also eliminate the need for equations (2.7), (2.8), and (2.21)–(2.24). The alternative expressions for $\mathbb{F}(t)$ and $\mathbb{T}(t)$ are restated below for convenience. They are written in the slightly altered yet equivalent and exact form

$$\mathbb{F}(t) = \mathbb{F}_s(t) + \mathbb{F}_u(t) + \mathbb{F}_w(t), \tag{A 1}$$

$$\mathbb{T}(t) = \mathbb{T}_s(t) + \mathbb{T}_u(t) + \mathbb{T}_w(t), \tag{A 2}$$

where the steady components of the normal force and torque are

$$\mathbb{F}_s(t) = -\tau(t)[\Gamma_{\pm}(t)]_-^+ \tag{A 3}$$

$$\mathbb{T}_s(t) = -\pi\,\tau(t)\nu(t), \tag{A 4}$$

the unsteady components of the normal force and torque are

$$\mathbb{F}_u(t) = \langle \dot{\Gamma}_+(t) \rangle_-^+ - \tfrac{\pi}{2}\dot{\alpha}_2(t), \tag{A 5}$$

$$\mathbb{T}_u(t) = \tfrac{3}{8}[\dot{\Gamma}_{\pm}(t)]_-^+ - \tfrac{1}{8}\pi\dot{\alpha}_3(t), \tag{A 6}$$

and the components of the normal force and torque that are induced by the presence of the circulation in the wake are

$$\mathbb{F}_w(t) = \frac{1}{2}(\beta_0 - \beta_2)[\Gamma_{\pm}(t)]_-^+ + \frac{\pi}{2}\sum_{n=2}^{\infty}\alpha_n(\beta_{n-1} - \beta_{n+1}), \tag{A 7}$$

$$\mathbb{T}_w(t) = \frac{1}{4}(\beta_1 - \beta_3)[\Gamma_{\pm}(t)]_-^+ + \frac{\pi}{2}(\alpha_0 - \alpha_2)\tau(t) + \frac{\pi}{4}\sum_{n=2}^{\infty}\alpha_n(\beta_{n-2} - \beta_{n+2}). \tag{A 8}$$

In Jones (2003), the real coefficients $\alpha_n(t)$ and $\beta_n(t)$ were defined implicitly in terms of two Chebyshev series expansions. However, it is possible to derive explicit expressions for $\alpha_n(t)$ and $\beta_n(t)$ and one can show that

$$\alpha_n(t) + \mathrm{i}\beta_n(t) = -\frac{1}{\pi}\left[\int_0^{\Gamma_{\pm}(t)}\delta_n(z_{\pm}(\Lambda, t))\,\mathrm{d}\Lambda\right]_-^+ \tag{A 9}$$

for $n = 0, 1, \ldots$, where

$$\delta_n(z) = \frac{(z - \sqrt{z+1}\sqrt{z-1})^n}{\sqrt{z+1}\sqrt{z-1}}. \tag{A 10}$$

REFERENCES

ANDERSEN, A., PESAVENTO, U. & WANG, Z. J. 2005 Unsteady aerodynamics of fluttering and tumbling plates. *J. Fluid Mech.* **451**, 65–90.

BAKER, G. R. & SHELLEY, M. J. 1990 On the connection between thin vortex layers and vortex sheets. *J. Fluid Mech.* **215**, 161–194.

BATCHELOR, G. K. 1967 *Introduction to Fluid Dynamics* Cambridge University Press.

BELMONTE, A., EISENBERG, H., & MOSES, E. 1998 From flutter to tumble: inertial drag and Froude similarity in falling paper. *Phys. Rev. Lett.* **81**, 345–348.

BIRKHOFF, G. 1962 Helmholtz and Taylor instability. *Proc. Symp. in Applied Mathematics*, vol. XIII. Am. Math. Soc.

DRAGHICESCU, C. I. & DRAGHICESCU, M. 1995 A fast algorithm for vortex blob interactions. *J. Comput. Phys.* **116**, 69–78.

FIELD, S. B., KLAUS, M., MOORE, M. G. & NORI, F. 1997 Chaotic dynamics of falling disks. *Nature* **388**, 252–254.

GREENGARD, L. & ROKHLIN, V. 1987 A fast algorithm for particle simulations. *J. Comput. Phys.* **73**, 325–348.

JONES, M. 2003 The separated flow of an inviscid fluid around a moving flat plate. *J. Fluid. Mech.* **496**, 405–441.

KRASNY, R. 1986*a* Desingularisation of periodic vortex sheet roll-up. *J. Comput. Phys.* **65**, 292–313.

KRASNY, R. 1986*b* A study of singularity formation in a vortex sheet by the point-vortex approximation. *J. Fluid Mech.* **167**, 65–93.

KRASNY, R. 1991 Vortex sheet computations: roll-up, wakes, separation. *Lectures in Applied Mathematics. Am. Math. Soc.* **28**, 385–401.

LINDSAY, K. & KRASNY, R. 2001 A particle method and adaptive treecode for vortex sheet motion in three-dimensional flow. *J. Comput. Phys.* **172**, 879–907.

LIU, J. & XIN, Z. 1995 Convergence of vortex methods for weak solutions to the 2-D Euler equations with vortex sheet data. *Commun. Pure Appl. Maths* **48**, 611–628.

MAHADEVAN, L. 1996 Tumbling of a falling card. *C. R. Acad. Sci. Paris,* II **323**, 729–736.

MAHADEVAN, L., RYU, W. S. & SAMUEL, A. D. T. 1998 Tumbling cards. *Phys. Fluids Lett.* **11**, 1–3.

MAXWELL, J. C. 1853 On a particular case of the decent of a heavy body in a resisting medium. *Camb. Dublin Math. J.* **9**, 145–148.

MITTAL, R., SESHADRI, V. & UDAYKUMAR, H. S. 2004 Flutter, tumble, and vortex induced autorotation *Theoret. Comput. Fluid Dyn.* **17**, 165–170.

MOORE, D. W. 1974 A numerical study of the roll-up of a finite vortex sheet. *J. Fluid Mech.* **63**, 225–235.

MOORE, D. W. 1975 The rolling up of a semi-infinite vortex sheet. *Proc. R. Soc. Lond.* A **345**, 417–430.

MOORE, D. W. 1979 The spontaneous appearance of a singularity in the shape of an evolving vortex sheet. *Proc. R. Soc. Lond.* A **365**, 105.

NITSCHE, M. & KRASNY, R. 1994 A numerical study of vortex ring formation at the edge of a circular tube. *J. Fluid Mech.* **97**, 239–255.

PULLIN, D. I. 1978 The large-scale structure of unsteady self-similar rolled up vortex sheets. *J. Fluid Mech.* **88**, 401–430.

PULLIN, D. I. & PERRY, A. E. 1980 Some flow visualisation experiments on the starting vortex. *J. Fluid Mech.* **97**, 239–255.

PULLIN, D. I. & WANG, Z. J. 2004 Unsteady forces on an accelerating plate and application to hovering insect flight. *J. Fluid Mech.* **509**, 1–21.

ROTT, N. 1956 Diffraction of a weak shock with vortex generation. *J. Fluid Mech.* **1**, 111–128.

SHELLEY, M. J. 1992 A study of singularity formation in vortex-sheet motion by a spectrally accurate vortex method. *J. Fluid Mech.* **244**, 493–526.

PESAVENTO, U. & WANG, Z. J. 2004 Falling paper: Navier-Stokes solutions, model of fluid forces, and centre of mass elevation. *Phys. Rev. Lett.* **93**, 144501-1–144501-4.

WILLMARTH, W. W., HAWK, N. E. & HARVEY, R. L. 1964 Steady and unsteady motions and wakes of freely falling disks. *Phys. Fluids* **7**, 197–208.